International Journal of Rock Mechanics & Mining Sciences 138 (2021) 104652

Contents lists available at ScienceDirect

International Journal of Rock Mechanics and Mining Sciences

journal homepage: http://www.elsevier.com/locate/ijrmms

Investigation of pillar damage mechanisms and rock-support interaction using Bonded Block Models

S. Sinha *, G. Walton

Geology and Geological Engineering, Colorado School of Mines, Golden, CO, United States

ARTICLE INFO

Keywords:
Rock pillars
Rock-support interaction
Bonded block models
Voronoi tessellation

ABSTRACT

In this study, Bonded Block Models (BBMs) are used to investigate the pillar damage mechanisms and rock-support interaction in massive-to-sparsely-fractured rockmasses. Hypothetical granite pillar models of width-to-height (W/H) ratio of 1, 2 and 3 are developed, and the input parameters are constrained by matching the stress-strain response of the BBMs to the stress-strain curves from FLAC3D models that were previously calibrated to an empirical pillar strength database. Two different block representations are also considered – elastic and inelastic. It was found that inelastic blocks are necessary to capture the behavioral transition from strain-softening to pseudo-ductile with increase in pillar W/H.

Post-calibration, different rockbolt combinations are tested in the BBM and their influence on the pillar strength and lateral deformations are analyzed. It was found that as the support density is increased, the peak pillar strengths also increase but the effect is dependent on the W/H. Deformation of the outer stress-fractured region and bulking systematically decreased with increasing support density, but the exact trend evolved as the pillars were loaded to various points on their stress-strain curves. Lastly, a BBM pillar was developed with explicit intra-block fracturing capability (i.e., individual blocks could break) and the support analysis was repeated. The goal was to understand if the continuum representation of damage within the inelastic blocks led to some underestimation of the rock-support interaction mechanism. It was ultimately concluded that the continuum inelastic representation of smaller-scale damage within individual blocks allows for a more appropriate representation of the rock-support interaction than the explicit intra-block representation.

1. Introduction

Pillars are an integral load bearing member in underground mines and play an important role in upholding the functional integrity of the mine openings. As mining progresses deeper and deeper, these pillars are subjected to even higher stresses, which increases the incidence and severity of ground control issues, including but not limited to spalling, buckling, pillar bursting, etc.[1,2] From a macroscopic failure standpoint, the design of pillars is well-studied[3–7] and typically involves consideration of a ratio of pillar strength to expected stress. On the contrary, design of skin supports for controlling stress-induced failures at the pillar periphery is not so straightforward, primarily because of our lack of understanding of the complex interaction between support elements and unsupported ground undergoing stress-induced damage. Some limited practical support guidelines, however, have been developed for mining and hard rock tunneling applications.[1,8]

The focus of this study is on brittle damage mechanics and rock-reinforcement interaction in highly stressed massive rockmasses, examined in context of mine pillars. The study of these topics is practically important in that it may ultimately lead to improved design of pillars and pillar support which will improve worker safety in underground mines. While field instrumentation (e.g. extensometer, stress cell, instrumented rockbolts, etc.) could be used for investigating these phenomena, such is expensive, time consuming and typically yields point estimates of rockmass response to loading.[9] An alternative tool for this purpose is the Bonded Block Modeling (BBM) technique, a subclass of Discrete Element Models (DEMs[10]), which represents a material domain by an aggregate of polygonal (Voronoi) or triangular (Trigon) blocks. These blocks can separate once the 'contacts' between the blocks fail in shear or in tension. Other discontinuum modeling tools like Particle Flow Code[11–13] or Finite Discrete Element Method[14–18] are commercially available and might have the potential to reproduce behaviors similar to those presented in this study. The current study, however, focuses specifically on understanding the capabilities of

* Corresponding author.
E-mail address: sankhaneelsinha@mymail.mines.edu (S. Sinha).

https://doi.org/10.1016/j.ijrmms.2021.104652
Received 6 June 2020; Received in revised form 6 January 2021; Accepted 6 January 2021
Available online 16 January 2021

Voronoi BBM, as implemented in Itasca's Universal Distinct Element Code (UDEC). Two major advantages of using Voronoi BBM in comparison to other available options are its well-established structural element suite (i.e. in UDEC[19–21]) and its ability to realistically simulate the tensile fracturing[22] and bulking process associated with brittle rock damage.[23]

To date, notable pillar-specific studies conducted using Voronoi BBMs include those by Preston et al.,[24] Bai et al.,[20] Muaka et al.[25] and Wang et al.[26] Preston et al.[24] evaluated the effect of height on the ultimate strength of jointed limestone pillars in Missouri using Voronoi BBMs. Instabilities related to water-rich roof layers in a Chinese coal mine were analyzed using entry-scale Voronoi models by Bai et al.[20] Muaka et al.[25] utilized the Voronoi approach to develop a methodology for designing jointed hard rock pillars that were transected by clay-filled shear zones. Wang et al.[26] studied the failure modes of coal pillars due to excavation of an adjacent underlying coal seam in China using the Voronoi approach. None of the previous studies, however, considered the influence of support in their models. Based on this, it is apparent that there is need for research focusing on assessment of rock-support interaction and intact rock bulking using Voronoi BBM.

Broadly speaking, the study of rock-support interaction embodies two key components: rockmass representation and support representation (each of these topics are discussed in the same order below). Rockmass representation deals with the replication of the macro-mechanical properties of the rock structure (in this case, a pillar) as well the underlying micro-mechanical processes. Once an appropriate rockmass representation is achieved, support can be incorporated in a given model and the resulting behaviors compared to those of its unsupported counterpart. For the purposes of this study, the only support considered is rockbolts, simulated using cable structural elements. Other discontinuum modeling studies (not employing Voronoi BBM) like Gao et al.,[19] Bai et al.[20] and Shreedharan and Kulatilake[27] have also used cable elements to model rockbolts.

In massive, highly stressed ground, damage occurs via brittle spalling along the pillar periphery[2,28,29] and via shearing inside the pillar core.[17] This is because closer to the periphery, the confining stresses are low, which promotes the development and growth of extensile fractures.[30] As one progresses inward, the propensity for extensile fracture development is suppressed due to the high confining stresses,[30] forcing the damage to occur in a shear mode. Such a change in failure characteristics as a function of position within the pillar is well documented in the literature.[17,31–34] As shearing is associated with sliding rather than separation, the associated bulking and dilation of the damaged rockmass is naturally lower than what is observed at the pillar periphery. It follows that a numerical model developed to simulate a rock pillar must be able to capture this transition in failure behavior.

Aside from the failure mode, another variable that plays an important role in modulating the macroscopic stress-strain response and the peak strength of pillars is its width to height ratio (W/H).[5,35–37] As the W/H is increased, the overall pillar behavior transitions from brittle to pseudo-ductile and the peak strength increases as well.

Sinha and Walton[38] previously attempted to model granite pillars (specifically Creighton granite from Sudbury, Canada) using Voronoi BBM, and in that study, the input parameters were constrained by matching the BBM stress-strain curves to stress-strain curves from a FLAC^{3D} model for W/H = 1, 2 and 3. A major drawback of that study is that the match to the stress-strain curves for W/H = 1, 2 and 3 were obtained with three different sets of BBM parameters, meaning that the parameters were not fundamental to the material being modeled. Sinha and Walton[38] attributed this issue to the elastic, unbreakable nature of the blocks in the BBMs. To remedy this problem and identify the optimal BBM representation for modeling granite pillars, we tested two options in this study – elastic blocks (same as in[38]) and inelastic blocks. The key difference between the two representations is that in the inelastic BBM, the constant strain triangular continuum zones used to discretize each block can yield and deform inelastically, while they can only deform in a linear elastic fashion in the elastic BBM.[39]

Inelastic BBMs are much more difficult to calibrate due to the large number of input parameters[40] and accordingly suffers from the parameter non-uniqueness issue.[41,42] To date, there have been few applications of inelastic BBM at the laboratory-scale[40,43,44] and at the field-scale.[45–49] Yang et al.[46,47] and Xue et al.[45] used entry-scale trigon models to examine the failure mechanisms around deep coal mine openings and refined the support patterns at the site. In Sinha and Walton,[48,49] observed pillar deformation trends in the Creighton mine and in the West Cliff coal mine were successfully reproduced, indicating that inelastic BBMs might have broader applicability. Note that the granite pillar BBM in Sinha and Walton[48] was subjected to a load path (both vertical and shear loading) from the calibrated mine-scale FLAC^{3D} model of Walton et al.[50] and was focused on the site-specific damage development in a pillar at Creighton mine. In contrast, the models presented herein are hypothetical, loaded purely in the vertical direction and attempt to simulate the progressive damage process of granite pillars for multiple W/H cases using a single parameter set, perhaps for the first time using polygonal BBM. The term 'hypothetical' means that the pillar BBMs do not correspond to any specific case study, but to the behavior of in-situ rock pillars in general.

The authors are unaware of any available field data that definitively indicates what aspects of the pillar behavior (beside dilatancy/bulking) are affected by the presence of support. One laboratory-based study that is relevant in this regard is that by Alejano et al.,[51] who attempted to quantify the reinforcement effect of pillar strapping by conducting laboratory tests on cabled specimens. They found that cabling reduced the lateral deformations and increased the residual strength, but did not have any notable effect on the peak strength. While this study enhances our understanding of rock-support interaction, it is limited to standard laboratory-scale specimens with only cable straps as means of support. Nevertheless, given that the specimens were slender (W/H = 0.5) in Alejano et al.,[51] one might expect similar changes in behavior with the addition of reinforcement to slender pillars. Such propositions cannot be made for W/H = 2 and 3 pillars that exhibit inelastic hardening prior to attaining their peak strengths.

In terms of numerical investigations of rock-support interaction, there is only a limited number of studies that have been conducted to date.[33,34,46,47,52] Gao et al.,[52] Kang et al.[33] and Yang et al.[46,47] presented a comparison of roof deflection with and without support in a coal mine entry, while Bai et al.34 presented some qualitative support guidelines for yielding coal pillars based on a discontinuum model (supports were not tested in the models). As a first step towards understanding the influence of reinforcement on ground behavior in numerical models, Sinha and Walton[23] employed the elastic W/H = 2 BBM from Sinha and Walton[38] to evaluate the effect of reinforcement on pillar behavior. In that study, different support patterns were tested with both Trigon and Voronoi block geometries. Unlike the Voronoi models, the Trigon models were found to show less of a reduction in bulking when supports were added than would be expected in reality. These and other models were used to also demonstrate how continuum models tend to underestimate the reinforcement effect of supports due to their enforcement of strain-continuity.

With respect to the support-analysis study of Sinha and Walton,[23] there are two main limitations concerning the pillar BBMs that were presented: (1) the fact that the input parameters used only applied to a specific W/H rather than the material more generally suggests that the model's predictive performance under differing conditions (i.e. with added support) may be poor; (2) the effect of reinforcement on the behavior of different W/H pillars was not analyzed.

To bridge the aforementioned gaps in the literature, the present study attempts to answer the following questions: (1) Is it possible to calibrate models for W/H = 1, 2 and 3 pillar cases with a single set of model parameters? (2) Can BBMs reproduce the pillar damage mechanisms described above? (3) How do rockbolts influence the strength and deformation of pillars? (4) Is the effect of rockbolts similar for different

W/H? (5) Does zone yield in inelastic BBM, which is a continuum representation of damage, lead to some underestimation of support effect?

2. Methods and model setup

In order to answer the first four research questions, rock damage and support effect were examined in the different W/H pillar BBMs. For the last question, we compared the reinforcement effect in the inelastic block model and an elastic block model, but the blocks in the elastic model were allowed to break along certain pre-defined failure pathways, thus representing the development of explicit damage within Voronoi blocks. This explicit block breakage technique has been previously employed by Gao et al.,[53] Wang and Cai[54] and Liu et al.[55] for laboratory-scale simulations.

Input parameters in BBMs are typically constrained by matching the macroscopic behavior of the model with those measured in laboratory or in field. Here, we used the stress-strain curves from the FLAC^{3D} granite pillar models presented by Sinha and Walton,[37] which in turn were calibrated to match the predicted peak strengths for multiple W/H pillar cases according to an empirical pillar strength database.[3,56,57] Accordingly, the calibrated BBM in this study also matches the empirical pillar strength predictions. By matching the peak strengths of unsupported BBMs to the empirical pillar strength prediction, it is effectively assumed that the pillars considered in the empirical strength database were unsupported or minimally supported. Although it is not explicitly mentioned in the relevant empirical studies that the pillars in question were unsupported, observations like peeling of the fractured wall material, sloughage up to the center of the pillar and recommendations to use cables and rockbolts to prevent the disintegration of fractured wall material seem to indicate that majority of the pillars were unsupported.[3,56,57] Lastly, as UDEC is a 2D software and simulates a plane-strain condition, the stress-strain curves for long pillars (length to width ratio of 4) were employed as the calibration targets.[58]

Fig. 1 shows the model setup used in this study. The edge length of each block was selected to be ~10 cm, as this is considered to be small enough so as to not impose any kinematic constraints on fracture development and growth. Field-scale models have historically used block sizes ranging from 6.5 cm to 50 cm.[20,22,24,26,59] Generally, BBM

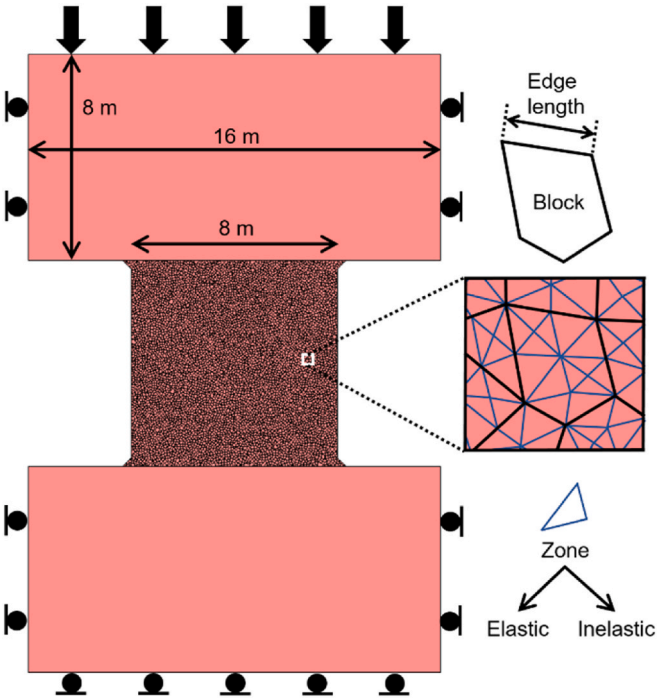

Fig. 1. Geometry and boundary conditions of the pillar model.

responses are dependent on the block size chosen, but for sufficiently small block sizes (such as that used in this study), changes in block size on the order of ~20% or less tend to not have much effect on the model response.[60]

For all three pillar geometries, the width of the pillar was set to 8 m and the height was varied to achieve the target W/H ratio. Loading was conducted via two elastic continuum beams on either side that are analogous to the roof and floor in an underground mine. Because in a typical mining scenario, pillars are strained mostly by the deflection of the immediate roof, we assigned a roller boundary to the bottom edge of the lower elastic beam and a very slow downward velocity to the top edge of the upper elastic beam. Additionally, to ensure homogeneity of the applied strain, the velocities were scaled with respect to the pillar W/H: 0.015 m/s for W/H = 1, 0.0075 m/s for W/H = 2 and 0.005 m/s for W/H = 3. These loading rates are small enough such that further reductions in loading rate do not affect the model response in any meaningful way. Loading was advanced in this pseudo-static manner until the peak strengths were attained in the different W/H pillar models.

UDEC discretizes each deformable block by multiple constant strain triangular 'zones'[39] (Fig. 1). These zones can be elastic or inelastic depending on the constitutive model assigned to them (referred to as 'elastic BBM' and 'inelastic BBM' in this study, respectively). For the inelastic BBMs, the Cohesion-Weakening-Friction-Strengthening (CWFS[61,62]) model was applied to the zones. This strength model essentially degrades the cohesive strength and mobilizes the frictional strength simultaneously or non-simultaneously as the plastic shear strain (ε_{ps}) increases, and is based on the fundamental extensile damage mechanism in brittle rocks.[30,63] Since its inception, the CWFS strength model has been employed by numerous authors to model the brittle rock damage process.[22,64–67]

Walton et al.[50] also used the CWFS strength model to simulate granite pillars (uniaxial compressive strength, UCS, of ~200 MPa) in Creighton mine, Canada. For rocks with similar UCS, the empirical pillar strength database, corrected numerically for length (i.e. for long pillars[58]), suggests that W/H = 1, 2 and 3 pillars in a UCS = 200 MPa granite should have peak strengths of 67 MPa, 116 MPa and 203 MPa, respectively. These values were therefore considered as the calibration targets for the BBMs in this study.

To calibrate the BBMs to the FLAC^{3D} stress-strain curves, pillar stresses and strains had to be recorded during the course of the model simulations. For that reason, vertical stresses averaged over all zones in the pillar and the displacements across the top and bottom edge of the pillar were tracked. The displacements were ultimately converted into strains by dividing them by the height of the pillar in question.

In UDEC BBM, the input parameters can be broadly subdivided into two groups: zone properties and contact properties. For elastic zones, the only parameters to be defined are Young's Modulus (E) and Poisson's ratio (ν), while for inelastic zones, additional strength parameters like peak and residual cohesion, peak and residual friction angle, peak and residual tensile strength, and critical ε_{ps} values that define the evolution of each of these strength components are needed. The Coulomb-slip behavior of the contacts is defined by normal and shear stiffness (j_{kn}, j_{ks}), peak and residual cohesion (c_{peak}, c_{res}), peak and residual friction angle (ϕ_{peak}, ϕ_{res}) and peak and residual tensile strength ($\sigma_{t,peak}$, $\sigma_{t,res}$). Unlike the zones, the drop from the peak to residual value for each strength component is instantaneous for the contacts.

In the supported models (Section 4), additional parameters corresponding to the cable structural elements were also defined (Table 1). These were chosen directly from Sinha and Walton,[23] who conducted simulated pull tests to match a load-displacement profile from Luke.[68] Cable element node spacing was set to 0.1 m to ensure that there was at least one node in each of the bolted blocks. It is noted here that node density can have some effect on model results as the algorithm for computing the interaction between rockbolts and the surrounding rock in UDEC depends on the location of the node within a zone. In our

Table 1
Input parameters for cable structural element.[23]

Parameters	Values
Diameter	0.024 m
Yield strength	3×10^5 N
Shear stiffness	2×10^9 N/m/m
Elastic Modulus	2.1×10^{11} Pa
Cohesive capacity of grout	3×10^5 N/m
Tensile strain limit	15%

experience, setting the node density such that one node occurs in each block leads to consistent results.[60] Rockbolt face plates (20 mm long, 5 mm thick) were simulated using beam structural elements.[39] These elements were assigned a modulus of 200 GPa, a Poisson's ratio of 0.25 and a rock-to-plate interface friction angle of 25°. All other interface strength properties were set to 0. To ensure effective load transfer between the rockbolts and the faceplates, the central node of each faceplate was attached to the last node of the corresponding rockbolt via an indestructible connection.

3. Pillar model results

3.1. Elastic block models

Elastic BBMs have a small number of input parameters and are relatively easy to calibrate. A manual back-analysis was conducted in this study to reproduce the FLAC^{3D} stress-strain curves from Sinha and Walton.[58] In this approach, individual parameters are first modified systematically to understand their influence on the stress-strain response, followed by changing multiple parameters at the same time. Table 2 lists the calibrated contact parameters and the respective stress-strain curves are shown in Fig. 2. Because not all points on the stress-strain curve can be considered to represent equally critically calibration targets, the use of R^2 or another quantitative measure of fit is not appropriate; instead, a qualitative comparison was performed. Accordingly, the obtained parameter combination does not necessarily represent the "best-fit" model, but rather one of several possible similar combinations that could all be considered reasonably calibrated.

A drop in the stress-strain curves immediately following yield is observed and is related to the brittle extensile fracturing along the periphery (temporary loss of load-carrying capacity) that pushed the stresses further into the pillar. Despite testing a variety of different parameter combinations, a match against the W/H = 1, 2 and 3 stress-strain curves with one set of input parameters could not be attained. This means that the parameters in Table 2 are not fundamental to the material being modeled (i.e. granite), and that an elastic block representation might not be appropriate to reproduce pillars behaviors of various W/H. Further explanation regarding the attempts to identify a single set of calibration parameters for all three elastic BBM W/H cases can be found in Appendix A.

Some interesting inferences can be made from the trends of the parameters in Table 2. W/H = 2 and 3 both required smaller contact tensile strengths in comparison to W/H = 1, likely because the slender geometry (W/H = 1) did not generate enough confining stress to suppress the tensile fracturing process. A steady decline in the peak cohesion value as a function of W/H is also consistent with the idea that frictional strength is important at larger W/H while the cohesive strength is more important for slender pillars. Lastly, ϕ_{res} had to be set to low values in order to prevent the geometric interlocking of the polygonal blocks as they are forced to rotate past one another.[69] If ϕ_{res} was raised over 12–13°, extremely large peak strengths for W/H = 2 and 3 and a large residual strength for W/H = 1 were obtained.

Table 2
Contact parameters for the elastic BBM.

Models	c_{peak}[a] (x10^6 Pa)	ϕ_{peak} (°)	ϕ_{res} (°)	$\sigma_{t,peak}$[a] (x10^6 Pa)	j_{kn} (Pa/m/m)	j_{ks} (Pa/m/m)
W/H = 1	120	34	5	40	10^{14}	5×10^{13}
W/H = 2	80	35	10	17.5	10^{14}	5×10^{13}
W/H = 3	50	46	8	17.5	10^{14}	5×10^{13}

[a] $\sigma_{t,res}$ and c_{res} were set to 0.

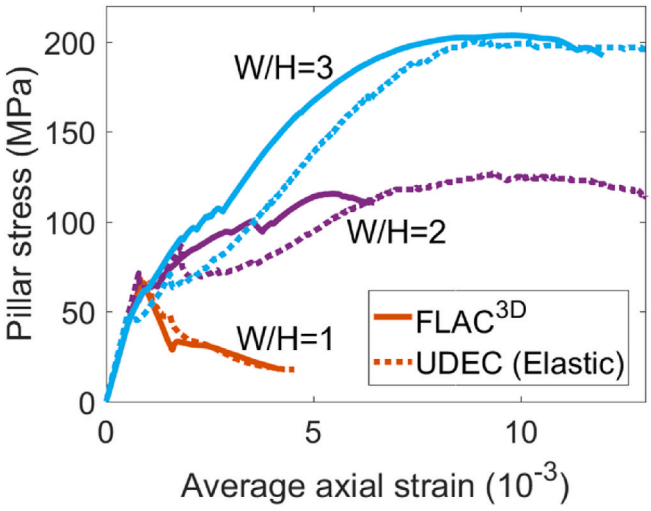

Fig. 2. Pillar stress-strain curves for W/H = 1–3 with elastic blocks.

3.2. Inelastic block models

The key to the successful implementation of the inelastic block representation is to allow the highly dilatant peripheral fracturing to occur explicitly via contact failure and the finer-scale shearing (limited dilatancy) inside the pillar via zone yield. This means that as the failure mode transitions from tensile to shear and the severity of localization decreases, the element within the BBM simulating the majority of the damage also changes from contact failure to zone failure. Such flexibility to replicate multiple damage mechanisms is not present in elastic BBMs, where failure can only occur via contact breakage.

Since in this study we are attempting to model granite pillars similar to those at Creighton mine, it was most logical to select the contact and zone strength properties from Sinha and Walton[48] as the starting point for calibration, followed by some minor modifications to account for the differences in loading path between the two studies. Table 3 lists the calibrated set of model parameters, and the corresponding stress-strain curves are shown in Fig. 3. These zone strength properties are very similar to those recommended by Walton[70] for a brittle rock with UCS of ~200 MPa and m_i of 20.9 (i.e. Creighton granite; see[70]). The only modification introduced in the CWFS strength model is the additional

Table 3
Contact and zone parameters for the inelastic BBM.

Zones - CWFS		Contacts	
E (Pa)	8×10^{10}	c_{peak} (Pa)	8×10^7
Peak cohesion (Pa)	5×10^7	c_{res} (Pa)	0
Residual cohesion (Pa)	4×10^6	ϕ_{peak} (°)	45
Peak friction angle (°)	0	ϕ_{res} (°)	16.5
Residual friction angle (°)	47.5	σ_t[a] (Pa)	17.5×10^6
Tensile strength (Pa)	25×10^6	j_{kn} (Pa/m/m)	10^{14}
Critical plastic shear strain from peak to residual	0.01	j_{ks} (Pa/m/m)	5×10^{13}

[a] $\sigma_{t,peak}$ was set to 0.

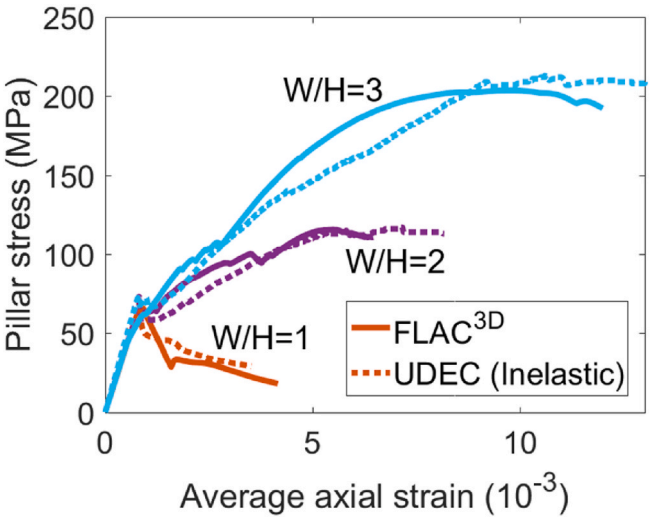

Fig. 3. Pillar stress-strain curves for W/H = 1–3 with inelastic blocks.

decay in the friction angle from 47.5° to 30° over a large critical plastic shear strain of 0.05. Such a decay was also reported by Martin and Chandler[63] and Renani and Martin[71] and is attributed to the loss of frictional strength due to destruction of asperities along initially rough stress-induced fracture surfaces. The small effective residual cohesive strength corresponds to stress-independent interlocking of rock fragments and/or rock-bridges that remain in the system after the initial fracturing has occurred.[70]

Contact parameters are less well-constrained based on prior study and were thus modified over a much wider range during the calibration process. In some cases, the physical meaning of the individual contact parameters is not as straightforward as might be assumed. For example, one might expect ϕ_{res} to be related to the basic friction angle in some fashion, but BBM behaviors are heavily influenced by the geometric interlocking of the blocks, meaning that values of ϕ_{res} less than the basic friction angle[72] are typically required.[22,73–75]

The calibrated inelastic BBM was able to successfully reproduce the peak strengths for all three W/H geometries and also the brittle response for W/H = 1 and strain-hardening behavior for W/H = 2 and 3 (Fig. 3). It was possible to obtain this behavior, especially for the W/H = 3 geometry, due to the gradual reduction of the zone friction angle for large critical plastic shear strains. In other words, deeper within the pillar where confining stress is high, failure occurs in a shear mode. Based on classical shear yield criteria, it is known that rocks lose strength following failure; this strain-softening behavior was implicitly modeled in the pillar 'core' by allowing the friction angle to degrade with increasing damage. Such a modification was not necessary in Walton et al.[50] and Sinha and Walton[48] because of the slender geometry of the pillars (W/H = 1.5) in those studies.

3.2.1. *Damage mechanisms in the model*

With the ability of the inelastic BBM to replicate the macroscopic strengths and behaviors of pillars with different W/H ratios established, further analysis was performed to ascertain if the underlying damage mechanisms were reproduced as well. Fig. 4 shows the failed contacts and yielded zones at various points on the stress-strain curves for each case. The following observations can be made based on the model results:

1. Damage in all the models initiates first by zone yield at the corners, followed by contact failure. Although the initial strength of the contacts is higher than that of the zones (Table 3), fracturing progressed via contact failure rather than zone yield along the pillar periphery due to point loading and wedging of blocks (Fig. 4b, f and 4h).
2. In the W/H = 1 pillar, even in the post-peak, the number of yielded zones is minimal, and pervasive contact damage can be noted throughout the entire pillar width. Indeed, the slender geometry prevents generation of high confining stresses within the pillar and failure consequently progressed via contact damage. The lack of core generation is evinced by the small region of yielded zones at the center of the W/H = 1 model (Fig. 4g).

To ensure that the failure of the contacts along the pillar periphery occurred in tension, the normalized number of tensile and shear cracks and yielded zones are plotted against pillar stress for the W/H = 2 geometry (see Fig. 5); corresponding plots for W/H = 1 and 3 are not shown, as they are similar to Fig. 5. It can be seen that when the stress-strain curve registers the onset of non-linear pillar behavior (between 'a' and 'b' in Fig. 4), the majority of the damage in the model has occurred by tensile cracking (refer to the blue circles in Fig. 5). For clarity, the plot of failed contacts at this loading state is also shown in the inset. From all this, we can infer that initial boundary cracking indeed occurred in a tensile mode, as one would expect in a massive brittle rockmass undergoing spalling.[2,30] It is also due to this reason that the W/H = 2 and 3 models exhibited a loss in load carrying capacity right after attainment of yield in both the elastic (Fig. 2) and the inelastic (Fig. 4) BBMs.

A secondary observation from Fig. 5 is that the number of contacts failing in shear starts to escalate immediately after this extensile failure phase in the inner portions of the pillar. Ultimately, the number of failed contacts levels off and zone shear becomes the dominant damage mode. Zone tensile failure plays a negligible role, as tensile failure occurs explicitly along the periphery and tensile stresses are suppressed deeper within the pillar.

4. Supported inelastic pillar models

In this section, we investigate how installation of rockbolts might influence the overall behavior of the three pillar W/H cases, and for that purpose, the three W/H models were re-run with different support combinations: (1) W/H = 1: 6 bolt and 10 bolt, (2) W/H = 2: 3 bolt, 5 bolt and 6 bolt, and, (3) W/H = 3: 3 bolt, 4 bolt and 5 bolt. In terms of bolt spacing, these support combinations correspond to (1) W/H = 1: 1.4 m and 0.78 m, (2) W/H = 2: 1.5 m, 0.75 m and 0.60 m, and, (3) W/H = 3: 0.83 m, 0.55 m and 0.42 m. For installing the rockbolts, a 0.5 m gap was left at the top and bottom of the pillar and the bolts were then spaced out in the vertical direction between these bounds. The idea was to prevent the installation of rockbolts very close to the pillar top and bottom, which is based on the operational constraints typically faced by a rock bolter in an underground mine.

To allow for easy comparison between the supported and unsupported models, support pressures were computed, following the equations provided by Hoek.[76] The equations in Hoek[76] correspond to the equivalent maximum pressures for support patterns, which represent the upper bound of what is mobilized in the field. Hoek[76] lists four equations for mechanical anchored rockbolts corresponding to 17 mm, 19 mm, 25 mm and 34 mm diameters and only one equation for 20 mm grouted rebar. As the resin grouted rockbolt in this study is 24 mm in diameter (chosen from [23]), the maximum support pressures computed from the mechanical bolt equations had to be used together with the 20 mm grouted rebar equation. Specifically, the equations for 20 mm and 24 mm diameter mechanical rockbolts were first determined via linear interpolation, and then the ratio of the support pressure for a 20 mm diameter mechanical rockbolt to the support pressure for a 20 mm diameter grouted rebar was applied to obtain the support pressure estimate for the 24 mm grouted rebar.

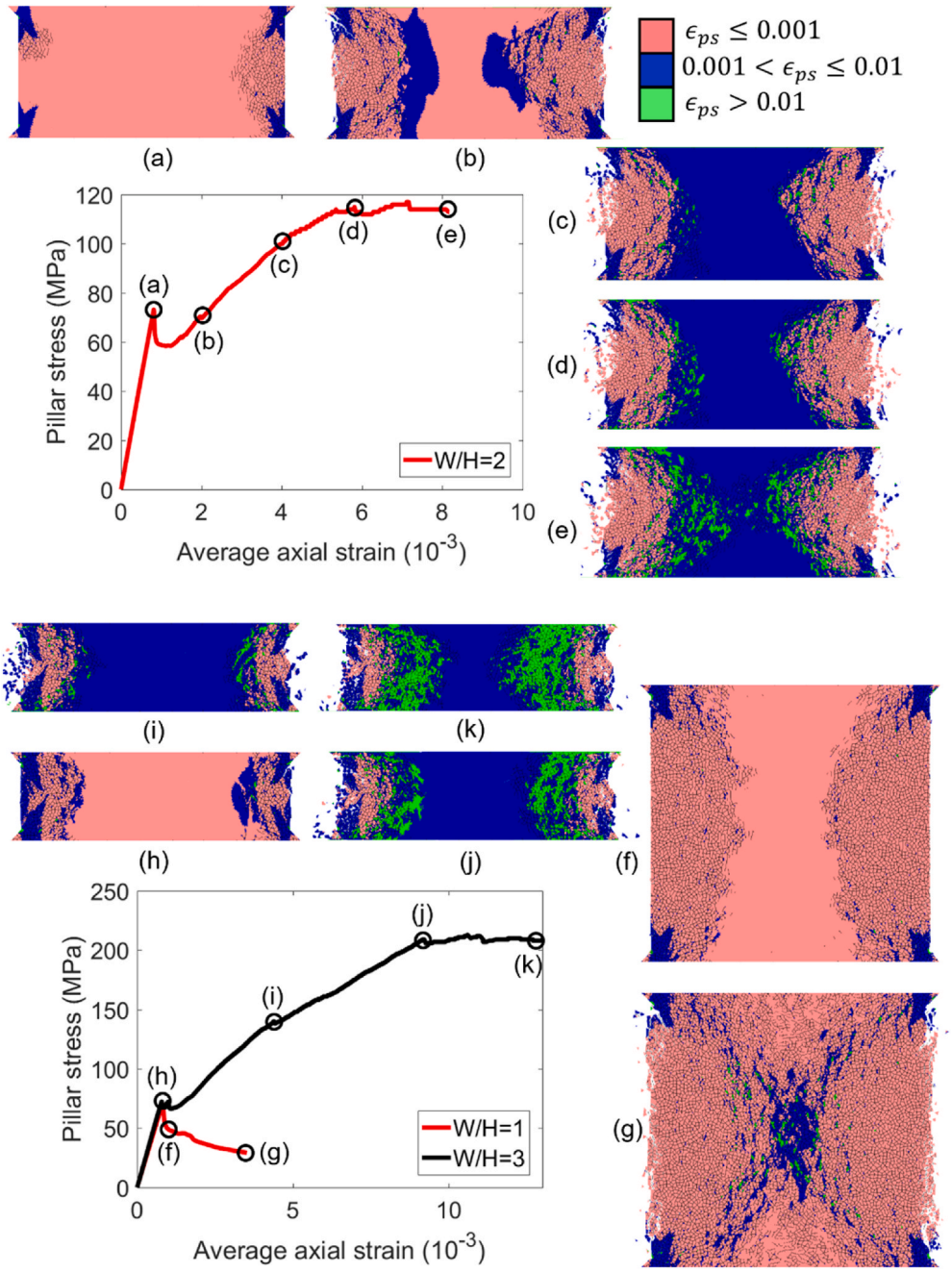

Fig. 4. Failed contacts and yielded zones at various stages of loading in the W/H = 1–3 pillar model.

3. For larger W/H cases, confining stresses are generated relatively early in the loading process, forcing the failure to occur through zone yield. In the late stages of loading (Fig. 4e, j and 4k), the intensity of zone damage starts to increase in the core. This intensity is greatest in the W/H = 3 model, as it is loaded to a larger total axial strain level. The depth of fractured contacts is also smaller in the W/H = 3 model in comparison to the W/H = 2 model at equivalent levels of axial strain. With continued loading, contact damage ultimately propagated all the way to the center of the pillar (Fig. 4e and k).
4. The transition from extensile cracking to shearing with depth is controlled by the W/H geometry, and this fundamental behavior is well captured in these models. The relative contribution of explicit contact damage and implicit zone damage towards the ultimate failure is also evident in Fig. 4.
5. Spalling and separation of blocks can be observed along the entire pillar periphery. The extent and severity of block detachment is greater in the larger W/H geometry models.

4.1. *Effect of support*

Fig. 6a shows the stress-strain curves for the most heavily supported BBM and the unsupported BBM for each W/H case. It is apparent from Fig. 6a that the overall response does not change very much with incorporation of support; the peak strengths, however, increase with increasing support density for the W/H = 2 and W/H = 3 pillars (Fig. 6b). As rockbolts pin the spalled slabs/blocks to the pillar, this generates some confinement, which would otherwise not be present if the failed rockmass is allowed to fracture and collapse into the adjacent excavations. From these results, it seems that the addition of support pressure has increased effect on squatter geometries (Fig. 6b), and this can be explained by the greater contribution of zone yield towards the ultimate failure of these pillar, combined with the fact that the gap in maximum principal stress between the peak and residual zone strength envelope increases at higher confining pressure (recall that the friction

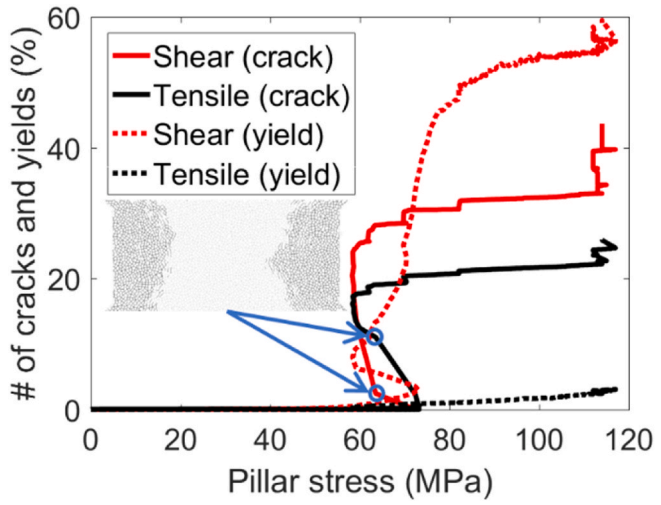

Fig. 5. Normalized number of failed contacts and yielded zones as a function of pillar stress for the W/H = 2 pillar model. Total numbers of contacts and zones in the model are 24310 and 34897, respectively.

angle of the peak and residual envelopes per Table 3 are 0° and 47.5°, and thus they diverge in the principal stress space).

Interestingly, for W/H = 1, the peak strength remains almost invariant, but the residual strengths increase with addition of support. This is consistent with the laboratory findings of Alejano et al.[51] for slender cabled laboratory specimens. A logical question with respect to the lack of a reinforcement influence on the W/H = 1 pillar peak strength is if rockbolts generate some amount of confining pressure on the periphery, then why does the strength remain unchanged, even though peak strength is well-known to increase with increasing confining stress[67,77,78]? The answer lies in the passive nature of the confining stress generated by rockbolts (and in the cabled samples of[51]) that is activated only when sufficient deformation (i.e. fracturing) had occurred in the rockmass. In laboratory tests with slender specimen geometries, large lateral deformations do not occur until the specimen is loaded to the post-peak,[79–81] and this is also observed in the current models. Consequently, any support-generated confinement can only influence the pillar behavior in the post-peak, as is evident in the W/H = 1 curves in Fig. 6.

Fig. 7 shows the horizontal displacements in the W/H = 2 unsupported and 5 bolt models at different loading stages. The depth and severity of fracturing increase as the unsupported pillar is strained monotonically by the two loading platens. With inclusion of 5 bolts, not only are the lateral displacements significantly suppressed, but so is the depth of fracturing. These results suggest that rockbolts can delay the inward propagation of fractures by generating local confinement (reinforce) and also efficiently pin and hold the spalled blocks, if the support density employed meets the appropriate strain demand. Of course, faceplates play an important role in controlling the surficial deformations by increasing the effective supported area of the pillar boundary.[82]

4.2. Bulking factor (BF)

Bulking factor is a convenient index for quantifying the effect of reinforcement and is defined as the increase in volume (or area in 2D) within the yielded/fractured region with respect to an undamaged state.[1,83,84] In physical terms, BF represents the dilation of the broken rockmass along the excavation boundary, and this index has found wide application in mining. For instance, one can estimate the approximate displacement demand on supports by multiplying a representative BF[1] with a semi-empirical estimate of failure depth.[85,86] It is important to note here that our previous study on rock-support interaction[23] treated the BF and the influence of support as independent of geometry or loading conditions, based on the rough empirical guidelines of Kaiser et al.[1] In this study, we computed the BFs for all the BBMs at various stages of loading.

The calculation was conducted for the supported and unsupported models at four distinct points (or analysis stages) along their strain-strain curves. Each of the four points correspond to four model step numbers; these numbers are the same in the unsupported and supported models with a particular W/H geometry. In other words, as the models are loaded by a constant downward velocity, choosing a fixed step number would mean that the outer surfaces of the loading platens also converged by a fixed amount. In-situ, this corresponds to a pillar that is being compressed/strained by the host rock following nearby production activities. The axial strains corresponding to the four analysis stages are listed in Table 4.

4.2.1. Calculation methodology

To compute the bulking factors, the following equation from Kaiser et al.[1] was employed:

$$BF = \frac{u_w - u_{d_f}}{d_f} \tag{1}$$

where, u_w is the displacement at the pillar edge, u_{d_f} is the displacement at the depth of failure, and, d_f is the thickness of the stress-fractured region. To obtain the three parameters, lateral displacements of all gridpoints (the vertices of the triangular zones) along multiple horizontal lines, spaced at 0.5 m vertically, were extracted from the BBMs.

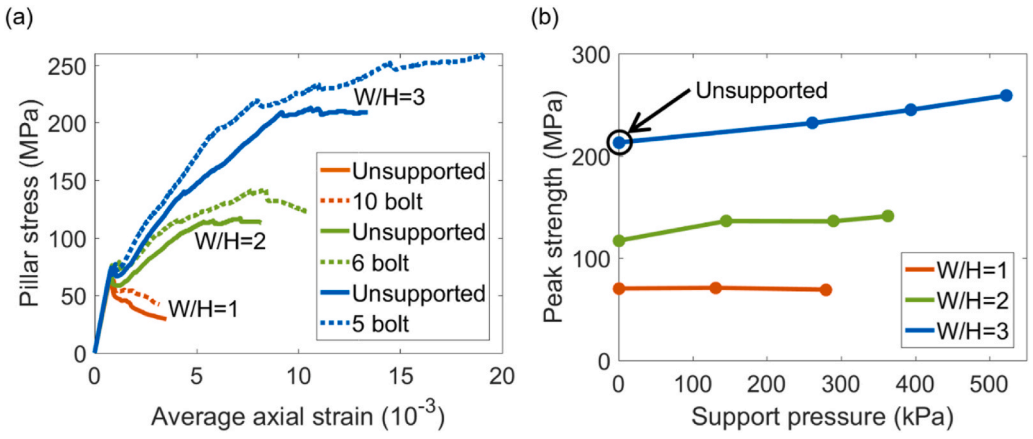

Fig. 6. (a) Stress-strain curves for the unsupported and most heavily supported models for W/H = 1, 2 and 3. (b) Peak strength as a function of support pressure for the unsupported and supported models. Zero support pressure corresponds to the unsupported model.

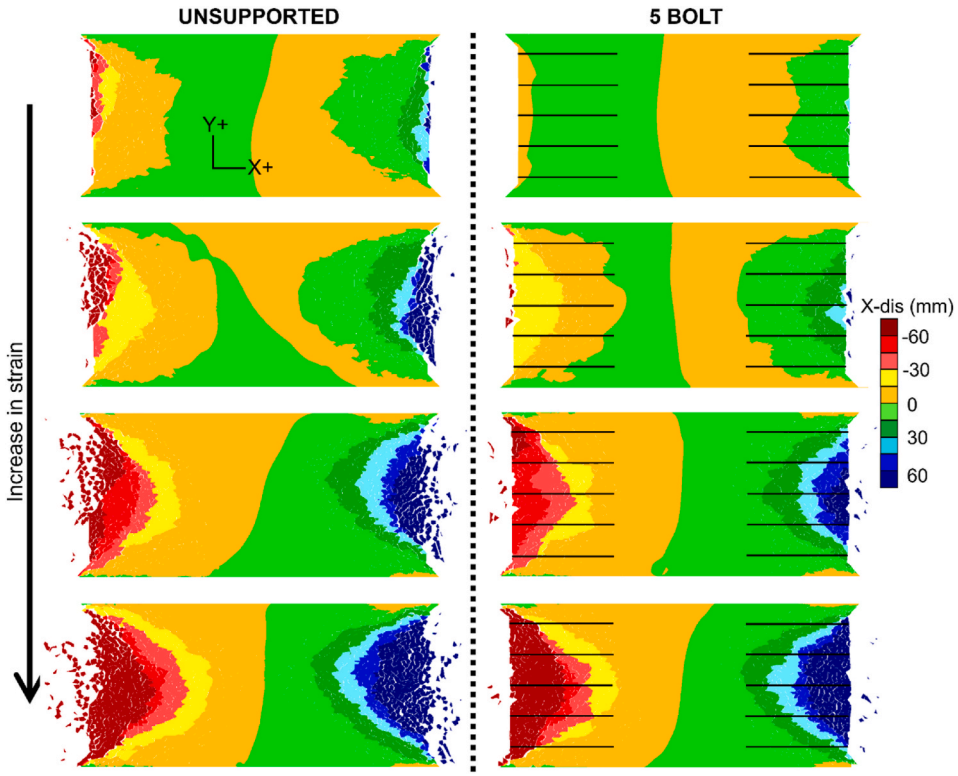

Fig. 7. Contour of horizontal displacement in the W/H = 2 pillar model without any bolts and with 5 bolts.

Table 4
Axial strains (10^{-3}) at which bulking factors are computed.

Stage	W/H = 1			W/H = 2				W/H = 3			
	Unsupported	6 bolt	10 bolt	Unsupported	3 bolt	5 bolt	6 bolt	Unsupported	3 bolt	4 bolt	5 bolt
1	1.13	1.02	1.00	2.14	1.95	1.89	1.90	2.96	2.74	2.58	2.66
2	1.70	1.53	1.52	4.05	3.81	3.78	3.68	4.67	4.33	4.07	4.23
3	2.67	2.36	2.36	5.56	5.22	5.30	5.31	6.47	6.00	5.78	5.53
4	3.52	3.29	3.28	7.16	6.93	6.69	6.72	9.19	8.97	9.20	8.91

These horizontal lines and the displacements along these lines (left half of the 8 m pillar) for one model are shown in Fig. 8. Using this figure as an example, u_w corresponds to the displacement at x = 0 for each line, d_f corresponds to the points where the displacement perturbations diminished and the curves became smooth (marked by black circles), and u_{d_f} corresponds to the lateral displacement at x = d_f. The methodology for determination of d_f and u_{d_f} is described in detail in Appendix B.

While a simpler approach would have been to determine the bulking factor along a single horizontal line along the pillar mid-height, such an approach would not be representative of the entire pillar, as the depth of fracturing is non-uniform (Fig. 7). Accordingly, bulking factor is computed along multiple lines, as shown in Fig. 8. To generate these displacement profiles, grid point addresses along the lines were extracted before running the models, followed by importing them back into the models at the four analysis stages (Table 4) to query the respective displacements. Because un-run model coordinates are used in the x-axis of Fig. 8, comparison to an undamaged state is implicitly accounted for in this calculation. Additionally, the subtraction in the numerator of Equation (1) accounts for both the explicit separation of blocks as well as the inelastic deformation within the zones, although the majority of the bulking observed in the models corresponds to explicit block separation.

This methodology is somewhat different from that used by Sinha and Walton[23] to compute the bulking factors. In that study, image analysis tool of MATLAB was employed to directly obtain the areal increase due to stress-fracturing from images of the BBM. Such an approach undoubtedly yields a more representative estimate of bulking factor, but could not be used in this study due to the large block separations observed at late stages of loading (Fig. 7). The separation of blocks made it challenging to identify a spatial domain over which to conduct the MATLAB image analysis.

4.2.2. Results and discussion

The results of the bulking factor analysis are summarized in Fig. 9 using two sets of graphs for each W/H case: BF versus inelastic axial strain and BF versus support pressure. Inelastic axial strain was obtained by simply subtracting the elastic strain, which is the pillar stress divided by the elastic modulus (80 GPa), from the total strain at the four analysis stages. The results from the BF analysis indicates a significant variation in the BF values for each model state analyzed (Fig. 9a, c, e). Generally, the BFs are larger at the pillar centers and are lower at the top and bottom edges. Some large BFs are, however, obtained at the pillar edges in cases where block separation had occurred (these regions also had lower d_f, thereby raising the BF).

BF increases with increasing inelastic axial strain, as expected, since inelastic axial strain serves as a damage index for the pillar as a whole. No consistent trend is observed in the data as a function of support pressure; some are concave, some are linear and some are convex. A divergence between the supported and unsupported bulking factors can

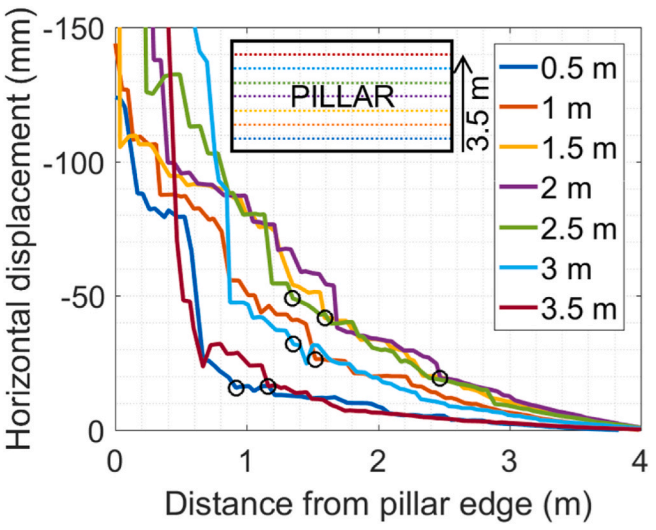

Fig. 8. Methodology for determination of bulking factor from horizontal displacement profiles. The numbers in legend represent the location of the horizontal lines from the base of the pillar. The black open circles represent the edges of the fractured region. The displacements correspond to the left half of the W/H = 2 unsupported model (Stage 4 in Table 4). All datapoints are spaced at 0.1 m along the x-axis.

be observed with increasing inelastic axial strain. The difference in BF between the unsupported and supported conditions is larger for the W/H = 1 and 2 models in comparison to W/H = 3. This means that supports are performing more efficiently in suppressing the dilation of the stress-induced fractures in these models.

In absence of any consistent non-linear relationship, a linear equation was fitted to the mean BF values as a function of inelastic axial strain. The R^2 values for all the fits are greater than 0.85. These equations were then employed to develop curves for BF versus support pressure at various inelastic axial strains, as shown in the right panels in Fig. 9. This interpolation based on the linear curve fits was required because the BFs for supported and unsupported models did not correspond to the same inelastic axial strain at the particular analysis stages considered (Fig. 9a, c, e). At low inelastic axial strain, the effect of rockbolts is negligible in the W/H = 1 model, as minimal lateral deformation occurred at this stage. With further increases in inelastic axial strain, the trend transformed into a near-exponential form, consistent with the empirical data of Kaiser et al.[1]

For W/H = 2, the BF support pressure relationship initially exhibited an exponential trend, but became linear between support pressures of 0 and 145 kPa at later stages of loading. It can be observed from Fig. 9d that the BF for the 3 bolt model (support pressure of 145 kPa) increases rapidly in comparison to the 5 bolt and 6 bolt cases (290 kPa and 363 kPa). A closer look at the model results indicated that the cable elements in the less supported model underwent grout failure and some of the elements in the central bolt also broke axially at later loading stages. Consequently, the rockbolts are not performing as effectively as the rockbolts in the 5 bolt and 6 bolt layouts. The W/H = 3 case exerted the greatest displacement demand on the support. Again, failure of cable elements was observed in the least supported model (3 bolt), which triggered the rapid increase in the BF observed in Fig. 9f. The 4 bolt and 5 bolt layouts did not exhibit any bolt breakage, but also had some grout failures. For that reason, the bulking factors increased more in these models with continued pillar damage than in the W/H = 2, 5 bolt and 6 bolt models.

The increasing demand on the support with increase in W/H is evident from the fact that the drop in BF between the unsupported condition and the intermediate support layout (i.e. 6 bolt for W/H = 1, 3 bolt for W/H = 2 and 3 bolt for W/H = 3) tapers off at large inelastic axial strain, even though the equivalent support pressures are greater. This is anticipated, as squatter pillars develop wider confined cores (minimal dilatancy in this region) and thus bulking concentrates more along the pillar periphery for a given amount of inelastic axial strain. Design of rock supports in grounds undergoing large deformation should therefore be based on balancing the anticipated displacement demand and the deformation capability of the support element.[8] As shown in Fig. 9, this displacement demand varies with loading, meaning that for an efficient support design, an estimate of surficial deformation over the functional life of the excavation is required.

Sinha and Walton[23] proposed a conceptual framework for the rock-support interaction. In that framework, the rock-support interaction curve, plotted in the support density - support pressure space, was split into three regions (Fig. 10): (i) Inadequate support region – Support density is not adequate and it breaks, leading to minimal effect on ground behavior; (ii) Maximum gain region – Increase in support density has the maximum marginal "value added" in this region with respect to some performance metric (e.g. BF reduction); and (iii) Overdesigned region – an excessive amount of support has been added to the system, and the effect of any further support on the ground is limited. With this framework in mind, it seems that at an inelastic axial strain of 0.007, the 10 bolt ($W/H = 1$) and 6 bolt ($W/H = 2$) models are either in the Overdesigned region or approaching the boundary between the Overdesigned and Maximum Gain regions; 6 bolt ($W/H = 1$), 5 bolt ($W/H = 2$), 4 bolt ($W/H = 3$) and 5 bolt ($W/H = 3$) models are in the Maximum Gain region; and 3 bolt ($W/H = 2$ and 3) models are either in the Inadequate segment or in the lower portion of the Maximum Gain region (Fig. 10). These classifications only apply to the specific loading condition considered, i.e. 0.007 strain. At lower inelastic axial strains, the 3 bolt ($W/H = 2$) model could be considered to be higher up in the Maximum gain segment, for example.

5. Elastic pillar models with explicit intra-block fracturing capability

In inelastic BBMs, fracturing within the blocks is approximated via zone yield. As zone yield is a continuum representation of damage and given that continuum models tend to underestimate the support effect,[23] there is a possibility that the support influence on pillar behavior reported in Section 4 is slightly underestimated relative to reality. To test this proposition, a BBM was developed that had explicit intra-block fracturing capability, and then the rock-support interaction analysis was repeated. The corresponding BBM is shown in Fig. 11a. This model is slightly different from the laboratory-scale BBMs of Gao et al.[53] and Liu et al.[55] that considered intra-block fracturing. In Gao et al.[53] and Liu et al.,[55] cracks were inserted between the block centroids and their vertices to further split the Voronoi blocks, while in this study, the BBM was first discretized by triangular zones and then the locations of the zone edges within each block were used to insert additional cracks within the BBM. This approach allowed more potential failure pathways to be introduced in the current BBM. The inter and intra-block contacts are shown by green and black lines in Fig. 11a.

The runtime of UDEC BBMs are dependent on the number of gridpoints and the contacts.[39] As these intra-block BBMs contain a large number of blocks, to attain an acceptable runtime, a symmetry condition was applied, and the zone size was set such that each triangular block corresponded to exactly one constant strain zone. This limited the number of gridpoints and contacts to be considered by the solution algorithm.

For determining if failure of the intra-block contacts could appropriately model the damage within blocks, the inter-block contacts were assigned the same properties as those listed in Table 3 and all blocks were made elastic, meaning that the only parameters considered for modification were those of the intra-block contacts. Despite numerous trials, a single set of parameters that could match the stress-strain curves for all three W/H geometries could not be identified, likely because of

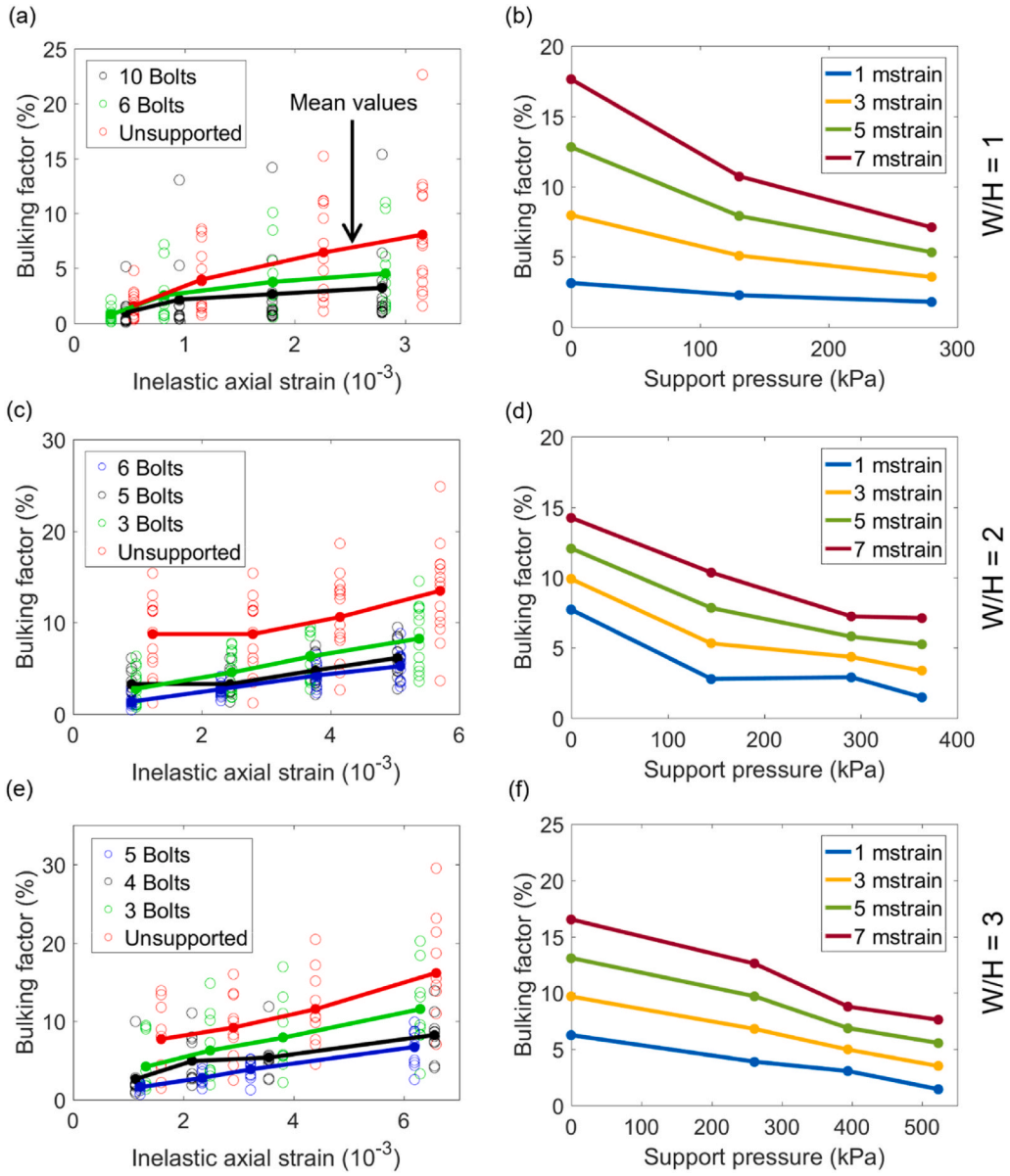

Fig. 9. Bulking factor as a function of inelastic axial strain for (a) W/H = 1, (c) W/H = 2, (e) W/H = 3, and, bulking factor as a function of support pressure for (b) W/H = 1, (d) W/H = 2, (f) W/H = 3. The solid lines in (a), (c) and (e) represent the mean BF values for each model at the different analysis stages. Greater support pressure corresponds to smaller spacing between the rockbolts.

the less complex nature of the contact constitutive model in comparison to the zone constitutive model. Accordingly, the support analysis was conducted using a BBM calibrated only to the W/H = 2 case. The intra-block contact properties for the calibrated model and a comparison of the stress-strain curve with the corresponding inelastic BBM are presented in Table 5 and Fig. 11b.

The explicit model was able to match the overall shape of the stress-strain curve. Fracturing in this model initiated by inter and intra block tensile cracking along the periphery, which later transitioned to intra-block shear failure at locations deeper within the pillar at late stages of loading (Fig. 12a). It is interesting to note how the intra-block contact strength properties are much larger than the inter-block ones (Table 3) yet internal damage progressed primarily via intra-block shearing. The reason for this behavior is the predisposition of triangular blocks or trigons towards shear fracturing due to the availability of linear failure pathways.[69,87] The horizontal deformation pattern in this model for the last recorded stage can be found in Fig. 12b.

For the rock-support interaction analysis, three support patterns were tested – 3 bolt (1.5 m spacing), 5 bolt (0.75 m spacing) and 6 bolt (0.60 m spacing). The stress-strain curves for these models are shown in Fig. 11b. Subsequently, bulking factors at four different model stages were computed for the unsupported, 3 bolt, 5 bolt and 6 bolt BBMs, followed by determining the bulking factors for different magnitudes of inelastic axial strain (as was done in Section 4.2). The results are illustrated in Fig. 13.

In comparison to the inelastic W/H = 2 BBM, it can be seen how the explicit model predicts higher strength gain with addition of supports: for the 5 bolt model, the strength increased by 19.7% and 16.2% in the explicit and the inelastic model, respectively, from their unsupported counterparts. The discrepancy is much larger in the lateral deformation behavior and bulking factor values. In particular, all explicit models exhibited low peripheral displacements due to the breakage of the Voronoi blocks into smaller triangles at late stages of loading. This is expected, as block breakage inhibits the development of large geometric mismatches in these models that are typically observed in Voronoi BBMs. The tendency of trigons to exhibit less volume changes in

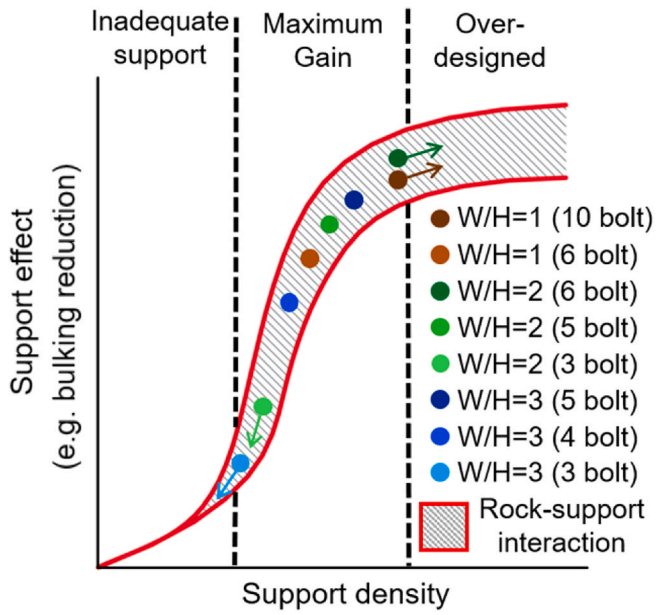

Fig. 10. The rock-support interaction curve and the location of the different supported BBMs on this curve at inelastic axial strain of 0.007. The arrows indicate the uncertainty in classification for some of the models. Greater support density corresponds to smaller spacing between the rockbolts.

comparison to Voronois under the same loading condition has been previously reported by Sinha and Walton.[23] Perhaps this issue could be overcome by sub-tessellating each Voronoi block with more Voronois, but this was not attempted for two reasons: (1) If the built-in Voronoi generator is used for this purpose, then very small Voronoi sub-blocks will be created. An alternate block generation technique is therefore required; (2) Since the sub-blocks are polygonal in shape, they will have to be discretized by multiple constant-strain zones, which will increase the model runtime drastically. For context, the elastic, inelastic and explicit W/H = 2 models took ~15–18 h, ~1 day and ~3–3.5 days to run, respectively, on a machine with a 10-core Intel i7-6950X processor and 64 GB of RAM. Depending on the number of sub-Voronois and the number of zones within each sub-Voronoi, we estimate a sub-tessellated model might take anywhere between 7 and 15 days to complete simulation on a similar machine.

Lastly, we compared the reinforcement effect in the inelastic and explicit BBMs by normalizing the bulking factors for the supported BBMs with respect to the unsupported bulking factors and these are listed in Table 6. Clearly, at all four inelastic axial strains, the drop in bulking factor with the addition of support is much larger in the inelastic BBM, suggesting that the bolts are performing more efficiently in suppressing the stress fractures in the inelastic BBM. It also seems that while allowing more explicit damage increases the influence of rockbolts, this increased effect might not be necessarily correct (more effect on strength rather than deformation, which is contrary to the experimental findings of[51]). The authors would like to reiterate that the results presented here are not just a manifestation of the BBM being semi-calibrated (i.e. calibrated to only one W/H stress-strain curve). This is because the inter-block properties are identical in both the explicit and inelastic model and the macroscopic axial behaviors are also almost identical, meaning that we have purely isolated the influence of the two different intra-block representations.

6. Conclusions

This study employed the Bonded Block Modeling (BBM) technique to simulate the progressive damage process of hard rock pillars and investigate the effect of reinforcement on pillar strength and deformability. Three different pillar BBMs with width to height (W/H) of 1–3

Table 5
Contact parameters for the intra-block contacts.

c_{peak}[a] (x10^6 Pa)	ϕ_{peak} (°)	ϕ_{res} (°)	$\sigma_{t,peak}$[a] (x10^6 Pa)	j_{kn} (Pa/m/m)	j_{ks} (Pa/m/m)
145	45	40	30	10^{14}	5×10^{13}

[a] $\sigma_{t,res}$ and c_{res} were set to 0.

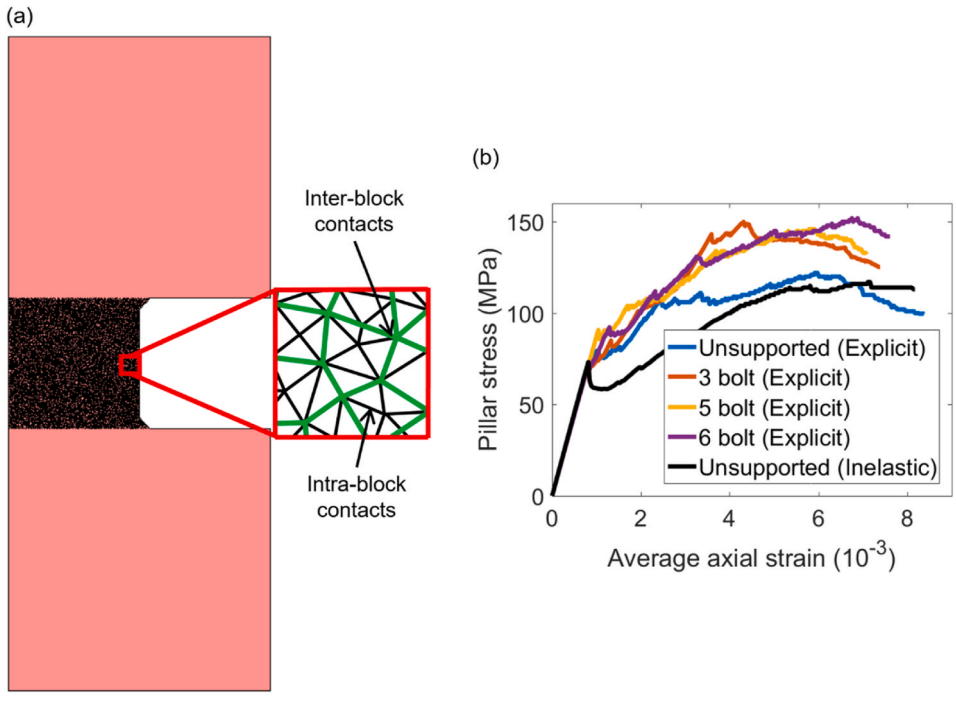

Fig. 11. (a) Geometry of the model with explicit intra-block fracturing capability, and (b) Stress-strain curves of different unsupported and supported BBMs.

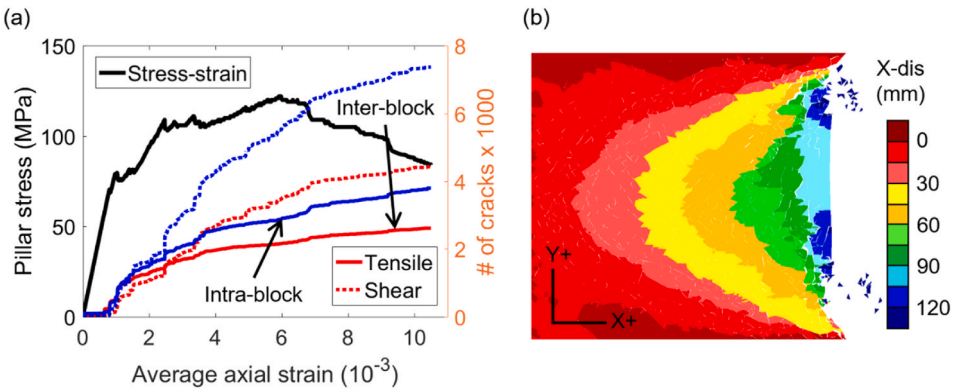

Fig. 12. (a) Crack count at various points along the stress-strain curve, and (b) Horizontal displacement contour for the W/H = 2 model at the terminal point of the stress-strain curve in (a). The total number of inter and intra-type contacts in this model are 9840 and 16022, respectively.

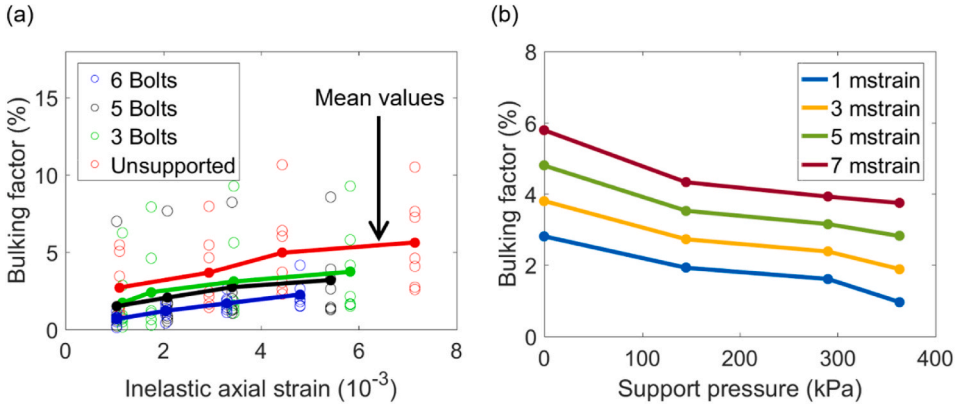

Fig. 13. (a) Bulking factor as a function of inelastic axial strain, and (b) bulking factor as a function of support pressure. The solid lines in (a) represent the mean BF values for each model at the different analysis stages. Greater support pressure corresponds to smaller spacing between the rockbolts.

Table 6
Comparison of normalized bulking factors in the inelastic BBM (Section 4.2) and in the BBM with explicit intra-block fracturing capability.

Inelastic BBM					BBM with intra-block fracturing				
Inelastic axial strain (10^{-3})	Normalized bulking factor (%)				Inelastic axial strain (10^{-3})	Normalized bulking factor (%)			
	Unsupported	3 bolt	5 bolt	6 bolt		Unsupported	3 bolt	5 bolt	6 bolt
1	100	36.1	37.6	19.3	1	100	68.6	57.4	34.3
3	100	53.7	43.9	34.0	3	100	71.7	62.7	49.7
5	100	64.9	48.0	43.4	5	100	73.6	65.8	58.8
7	100	72.7	50.8	49.9	7	100	74.8	67.8	64.7

were developed and calibrated to match the stress-strain curves from previously calibrated FLAC3D models. Both elastic and inelastic blocks were tested. Results indicated that it is necessary to consider inelasticity within the blocks in order to reproduce both the target stress-strain curves and the transition in damage mode from low confinement brittle fracturing along the periphery to confined shearing deeper within the pillar. The inelastic BBM was subsequently used for support analysis, whereby the peak strengths and lateral deformations (quantified by the 'bulking factor') in models with varying rockbolt densities were compared. Unlike the W/H = 2 and 3 models, the peak pillar strength remained relatively unaffected in the W/H = 1 model with inclusion of support; the residual strengths, however, increased with increasing support density in all cases. The bulking factors evolved as each pillar BBM was progressively loaded up to failure, and at any given loading stage, the bulking factors were lower in the models with higher support density. The exact trends differed as a function of the W/H ratio. These results indicate that the support influence varies depending on the geometry and loading conditions of a pillar.

Previous studies have shown that continuum models tend to underestimate the reinforcement effect of supports. As inelastic yield within blocks is also a continuum approximation of damage, it is possible that the support influence on ground behavior observed from the inelastic BBM might be slightly underestimated. To test this hypothesis, an elastic BBM was developed with explicit intra-block fracturing capability (polygonal blocks sub-divided into numerous triangular blocks), and the support analysis was repeated with this model. Contrary to expectation, it was found that when more damage was allowed to develop explicitly within the blocks, the influence of supports increased in terms of peak strength but reduced in terms of displacement suppression. This finding was explained by the inability of the triangular block assemblage to dilate in a realistic manner as compared to polygonal block assemblies.

Declaration of competing interest

The authors declare that they have no known competing financial interests or personal relationships that could have appeared to influence the work reported in this paper.

Acknowledgement

The research conducted for this study was funded by the National Institute for Occupational Safety and Health (NIOSH) under Grant Number 200-2016-90154. The authors would like to extend their gratitude for the financial support. Special thanks to Dr. Mark Larson, Dr. Bo-Hyun Kim and Isabella West for reviewing this manuscript prior to submission and providing valuable suggestions. The modeling effort for this study was conducted using educational licenses of UDEC provided by Itasca Consulting, Ltd. The authors appreciate Itasca's support in this capacity.

Appendix A. Elastic block calibration trial results

To demonstrate that it was indeed not possible to obtain a single set of elastic BBM parameters that could match the stress-strain curves for all 3 W/H geometries, some illustrative model results for the W/H = 1 and 3 BBMs are presented here. These two geometries were chosen for illustration as they have different failure modes – W/H = 1 fails primarily by tensile fracturing while W/H = 3 fails primarily by shearing.

Out of the many different parameter combinations tested as a part of the calibration process for the W/H = 1 BBM, 9 key combinations and their peak strengths are shown in Table A1 (Model 1 is the base parameter set from which the calibration started). The corresponding stress-strain curves can be found in Fig. A1For this model, the target peak strength per the empirical database from the literature is 67 MPa, and the target stress-strain response is indicated by the black line in Fig. A1. It can be observed from Table A1 and Fig. A1 that an increase in both the $\sigma_{t,peak}$ and c_{peak} (compare Models 1 and 6) was necessary in order to attain a peak strength of ~70 MPa. Individually raising c_{peak} (compare Models 1 and 2) or $\sigma_{t,peak}$ (compare Models 1 and 7) or changing other input parameters like ϕ_{peak} (Model 3) did not produce the desired effect. Additionally, in models where $\sigma_{t,peak}$ was 40 MPa, the post-peak strengths were relatively high (Fig. A1), and a lowering of ϕ_{res} to 5° was necessary in order to reproduce the target stress-strain curve (compare Models 6 and 8).

Table A1
Different parameter sets tested for the W/H = 1 elastic BBM. Target W/H = 1 strength is 67 MPa.

Model	c_{peak}* ($x10^6$ Pa)	ϕ_{peak} (°)	ϕ_{res} (°)	$\sigma_{t,peak}$* ($x10^6$ Pa)	Peak strength ($x10^6$ Pa)
1-Base	80	30	10	17.5	39
2	120	30	10	17.5	48
3	120	40	10	17.5	59
4	140	30	10	17.5	54
5	120	30	10	25	53
6	120	30	10	40	69
7	80	30	10	40	53
8	120	30	5	40	58
9 - Calibrated	120	34	5	40	68

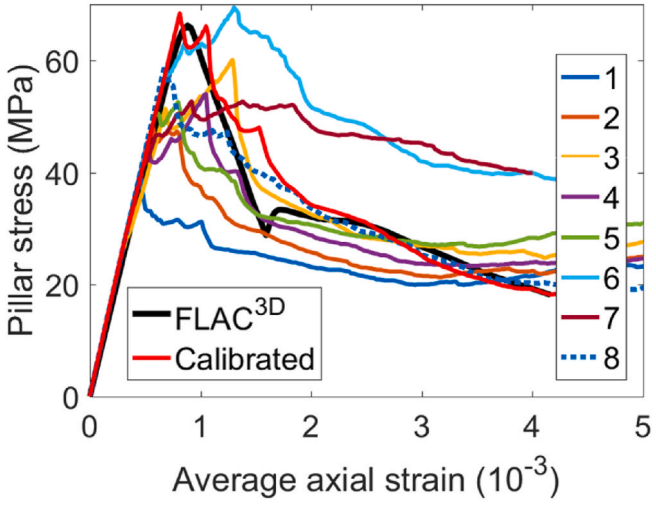

Fig. A1. Stress-strain curves for Models 1–9 with W/H = 1.

For the W/H = 3 geometry (Table A2), the base parameter set overestimated the target peak strength and any increase in c_{peak} (Model 3) only increased the mismatch (Fig. A2a). ϕ_{res} had a substantial effect on the model results, and the peak strength reduced to 151 MPa (Model 2) when the model was run with the calibrated parameters for the W/H = 1 geometry. Note how all the input parameters of Model 2 are larger than Model 1 in Table A2 except ϕ_{res}, yet the strength reduced by 31%. Given that Model 2 followed the target stress-strain curve up to ~150 MPa (Fig. A2a) and then deviated (due to low ϕ_{res}), one might wonder if it is possible to attain the target peak strength by just increasing ϕ_{res}.

Table A2
Different parameter sets tested for the W/H = 3 elastic BBM. Target W/H = 3 strength is 203 MPa.

Model	c_{peak}* (x10^6 Pa)	ϕ_{peak} (°)	ϕ_{res} (°)	$\sigma_{t,peak}$* (x10^6 Pa)	Peak strength (x10^6 Pa)
1-Base	80	30	10	17.5	219
2	120	34	5	40	151
3	100	30	10	17.5	235
4	120	34	8	40.0	194
5-Calibrated	50	46	8	17.5	201

To that end, we ran one more model with ϕ_{res} of 8° (Model 4). While this model could reproduce the target strength within 10 MPa, large mismatches occurred along the majority of the stress-strain curve. The corresponding W/H = 1 model had a peak strength of 72 MPa. To further emphasize the effect of employing such large values of c_{peak} and $\sigma_{t,peak}$, the stress-strain curves for the W/H = 2 BBM with parameter sets 2 and 4 in Table A2 are shown in Fig. A2(b). Clearly, the target trend is not being reproduced, and the mismatch only increases with increasing ϕ_{res} (Models 2 and 4). Based on this, it seems that it might be possible to reproduce only the target strengths, but not the complete stress-strain curves with a single set of input parameters, because W/H = 2 and 3 require lower c_{peak} and higher ϕ_{res}, while W/H = 1 requires higher c_{peak} and $\sigma_{t,peak}$, and lower ϕ_{res}.

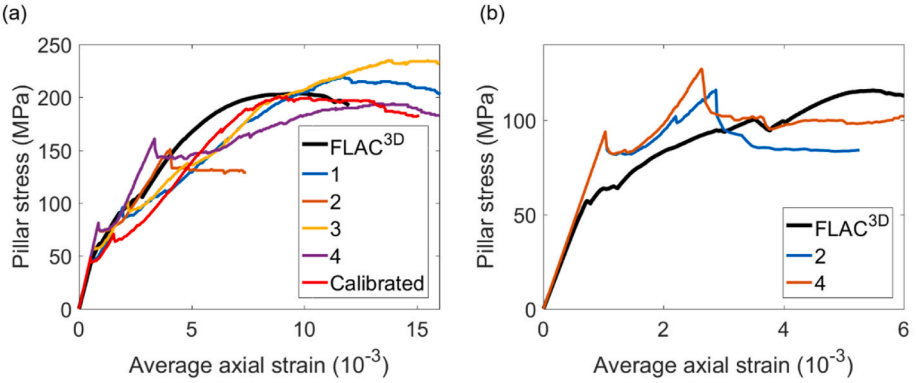

Fig. A2. (a) Stress-strain curves for Models 1–5 with W/H = 3, and (b) Stress-strain curves for W/H = 2 with model parameter sets 2 and 4 in Table A2.

Appendix B. Bulking factor calculation details

In the initial stages of analysis, d_f was identified manually, but it became increasingly difficult to determine d_f, especially in the supported models, where either the sudden jump in displacement was preceded by a section with inconsistent curvature or there was no sudden jump at all. To overcome this issue, a criterion was developed to automatically detect d_f based on the average slope between every three adjacent displacement datapoints, referred to as *disp slope* (all datapoints were spaced at 0.1 m). d_f was defined to correspond to the maximum distance from the pillar edge where a particular threshold value of this average slope is exceeded. Based on visual inspection of multiple lateral displacements and slope profiles, a *disp slope* threshold of 60 mm/m was selected. The black open circles in Fig. 8 were automatically identified using this threshold approach.

Determination of an appropriate u_{d_f} also required some interpretation, particularly in cases where blocks have detached from the pillar surface. Some examples of how this separation process appears in the displacement profiles is provided in Figs. 7 and 8 (heights of 2 m, 2.5 m, 3 m, and 3.5 m). Since bulking factor is a continuum concept, in that it assumes the system to behave as a continuous body, utilizing the large displacements of the detached blocks is inappropriate. This is reflected in the fact that the bulking factors in Kaiser et al.[1] for unsupported conditions were based on observations in the floor, where gravitational forces prevented any significant block detachment. Since our focus is on pillar behavior rather than the floor, a different approach was required.

We compared various displacement profiles and model plots and determined that when the displacement difference between two adjacent datapoints was greater than ~50 mm (corresponds to a strain threshold of 0.5), this tended to correspond to blocks that the authors would judge to have fully separated. To simplify the bulking analysis, we disregarded all peripheral displacements beyond the point at which the threshold was exceeded and considered the displacement gradient to be 0.5 m/m in this remaining space. Physically, this implies that the region consisting of separated blocks is effectively replaced with an equivalent continuum region having a constant strain of 0.5. This is undoubtedly a simplified approach, but in absence of any well-defined methodology for calculating bulking factors in discontinuum models, such an approach serves as a useful starting point.

When the two approaches outlined above were employed for calculating the bulking factors at the four analysis stages (Table 4), an issue was encountered. In particular, as the lateral displacements and depths of fracturing are smaller in the early phase of loading, the corresponding d_f values were also smaller. With continued loading, fractures propagated deeper into the pillar and d_f increased. In context of Eq. (1), there are therefore two competing elements – the difference in displacements at the pillar wall and at x = d_f, and d_f, both of which increase with loading and ultimately control the bulking factor. Intuitively one would expect the bulking factor to either increase or remain constant with loading, but in some of our models, the bulking factor decreased due to the d_f increasing at a faster rate than $u_w - u_{d_f}$. To resolve this issue, we computed d_f only for the last analysis stage (Stage 4) and used this value for the rest of the loading stages. This led to a systematic increase in the bulking factor values as the pillar was progressively strained. It should be recognized here that Kaiser et al.'s[1] BF estimates do not acknowledge the progressive nature of BF as damage develops with continued loading.

Given the dependence of the BF calculation on user-selected parameters, a sensitivity analysis was conducted on the strain gradient threshold and *disp slope* threshold, and the corresponding W/H = 2 unsupported model BFs are shown in Figs. B1(a, b). The BFs increased with increases in both the

strain gradient threshold and the *disp* $_{slope}$threshold; this is expected, as the first threshold raises $u_w - u_{d_f}$ while the latter lowers d_f. The mean values appear to follow an approximately linear trend with a positive slope. Similar analyses were also conducted for the supported models, but the changes were minimal when the strain gradient was varied, while a reduced effect was noted with changes in the *disp* $_{slope}$threshold. Supported models tended to be more continuous along the pillar edge and hence the application of the strain gradient threshold was mostly limited to the unsupported models. This is illustrated by the displacement profiles along the pillar mid-height for the W/H = 2 unsupported, 3 bolt, 4 bolt and 5 bolt BBMs (Fig. B1c).

Although the sensitivity analysis shows that the strain gradient threshold and the *disp* $_{slope}$ threshold has some effect on the computed BF, their influence is not practically significant. Accordingly, if for example a *disp* $_{slope}$ threshold of 50 mm/m is ultimately judged to be more appropriate than our final analysis value of 60 mm/m, then such a choice does not invalidate the results presented in this study.

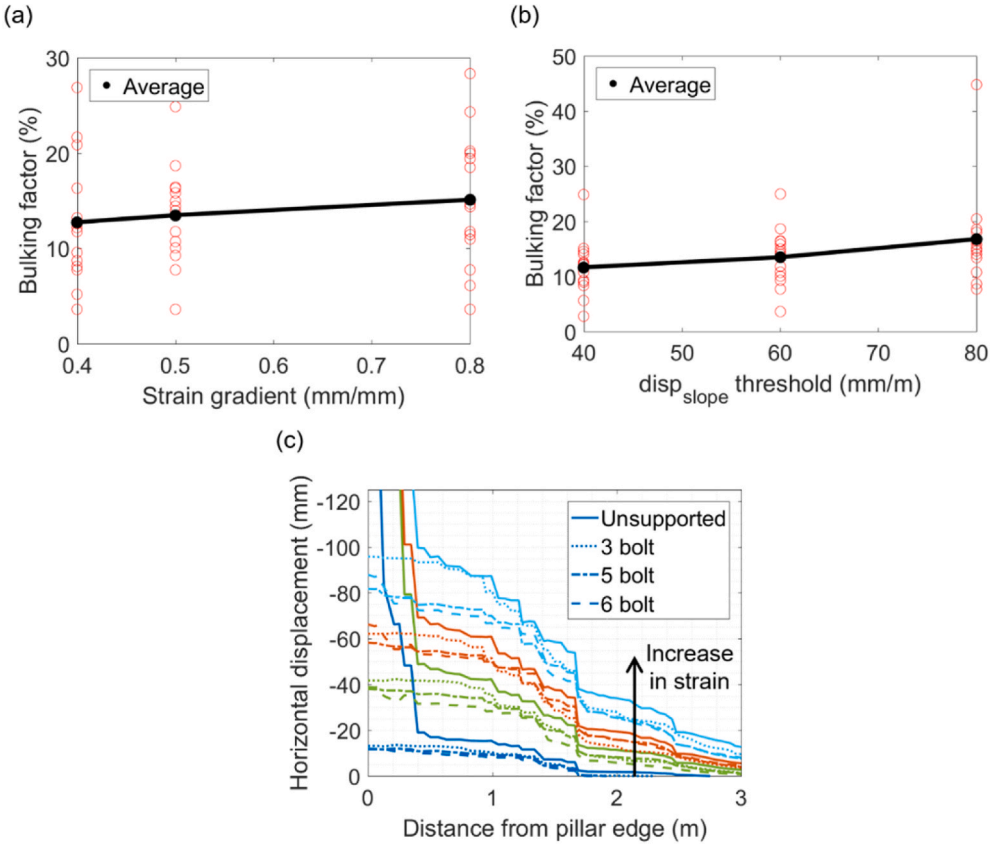

Fig. B1. Sensitivity of the (a) strain gradient threshold, (b) *disp* $_{slope}$ threshold on the computed bulking factor for the W/H = 2 unsupported model, and (c) Horizontal displacement profiles (left side) along the pillar mid-height for the W/H = 2 BBMs at different loading stages. Strain gradient of 0.5 and *disp* $_{slope}$ threshold of 60 mm/m was employed for the final analysis.

References

1 Kaiser PK, McCreath D, Tannant D. *Canadian Rockburst Support Handbook*. Geomechanics Research Center and CMIRO Sudbury, Canada; 1996.
2 Diederichs MS. The 2003 Canadian Geotechnical Colloquium: Mechanistic interpretation and practical application of damage and spalling prediction criteria for deep tunnelling. *Can Geotech J*. 2007;44(9):1082–1116.
3 Hedley DGF, Grant F. Stope-and-pillar design for the elliot lake uranium mines. *Bull Can Inst Min Metall*. 1972;63:37–44.
4 Krauland N, Soder PE. Determinating pillar strength from pillar failure observations. *Eng Min J*. 1987;8:34–40.
5 Martin CD, Maybee WG. The strength of hard-rock pillars. *Int J Rock Mech Min Sci*. 2000;37(8):1239–1246.
6 Potvin Y, Hudyma MR, Miller HDS. Design guidelines for open stope support. *Bull. Can. Min. Metall.* 1989;82:53–62.
7 Lunder PJ, Pakalnis R. Determination of the strength of hard-rock mine pillars. *Bull Can Inst Min Metall*. 1997;90:51–59.
8 Kaiser PK. *From common to best practices in underground rock engineering. Proceedings of the 14th International Congress on Rock Mechanics and Rock Engineering*. Brazil: Foz do Iguassu; 2019:141–179.
9 Forbes B, Vlachopoulos N, Diederichs MS, Hyett AJ, Punkkinen A. An in-situ monitoring campaign of a hard rock pillar at great depth within a Canadian mine. *Journal of Rock Mechanics and Geotechnical Engineering*. 2020;12:427–448.
10 Cundall PA. A computer model for simulating progressive large-scale movements in blocky rock systems. *Proceedings of International Society for Rock Mechanics Symposium: Rock Fracture, France*. 1971:129–136.
11 Cai M, Kaiser PK, Morioka H, et al. FLAC/PFC coupled numerical simulation of AE in large-scale underground excavations. *Int J Rock Mech Min Sci*. 2007;44(4):550–564.
12 Kias MEC, Ozbay U. Modeling unstable failure of coal pillars in underground mining using the discrete element method. In: *Proceedings of 47th US Rock Mechanics/ Geomechanics Symposium, San Francisco, US*. 2013. Paper No. 174.
13 Wanne T, Johansson E, Saanio DP. *Äspö Pillar Stability Experiment Final Coupled 3D Thermo-Mechanical Modeling and Preliminary Particle-Mechanical Modeling*. SKB; 2004. Report R-04-03.
14 Elmo D, Stead D. An integrated numerical modeling - discrete fracture network approach applied to the characterization of rock mass strength of naturally fractured pillars. *Rock Mech Rock Eng*. 2010;43(1):3–19.
15 Lisjak A, Figi D, Grasselli G. Fracture development around deep underground excavations: insights from FDEM modelling. *Journal of Rock Mechanics and Geotechnical Engineering*. 2014;6(6):493–505.
16 Lisjak A, Kaifosh P, He L, Tatone BS, Mahabadi OK, Grasselli G. A 2D, fully-coupled, hydro-mechanical, FDEM formulation for modelling fracturing processes in discontinuous, porous rock masses. *Comput Geotech*. 2017;81:1–8.
17 Li X, Kim E, Walton G. A study of rock pillar behaviors in laboratory and in-situ scales using combined finite-discrete element method models. *Int J Rock Mech Min Sci*. 2019;118:21–32.
18 Vazaios I, Diederichs MS, Vlachopoulos N. Assessment of strain bursting in deep tunnelling by using the finite-discrete element method. *Journal of Rock Mechanics and Geotechnical Engineering*. 2019;11(1):12–37.
19 Gao F, Stead D, Kang H. Numerical simulation of squeezing failure in a coal mine roadway due to mining-induced stresses. *Rock Mech Rock Eng*. 2015;48:1635–1645.
20 Bai Q, Tu S, Zhang C, Zhu D. Discrete element modeling of progressive failure of wide coal roadway from water-rich roofs. *Int J Coal Geol*. 2016;167:215–229.

21 Bahrani N, Hadjigeorgiou J. Explicit reinforcement models for fully-grouted rebar rock bolts. *Journal of Rock Mechanics and Geotechnical Engineering*. 2017;9(2):267–280.
22 Dadashzadeh N. *Reliability of Stress Induced Damage Predictions in Hard Rocks with Continuum and Discontinuum Numerical Modelling Approaches. PhD Thesis*. Canada: Queen's University; 2020.
23 Sinha S, Walton G. Understanding continuum and discontinuum models of rock-support interaction for excavations undergoing stress-induced spalling. *Int J Rock Mech Min Sci*. 2019;123:104089.
24 Preston RP, Stead D, McIntire H, Roberts DP. Quantifying the effects of adverse geology on pillar strength through numerical modeling. In: *Proceedings of 47th US Rock Mechanics/ Geomechanics Symposium, San Francisco, California, US*. 2013. Paper No. 478.
25 Muaka JJ, Duma S, Mushangwe P, et al. *Modelling hard rock jointed pillars using a distinct element and discrete fracture network approach considering the effect of a clay-filled shear structure*. Perth, Australia. *Proceedings of the 8th International Conference on Deep and High Stress Mining*. 2017:311–328.
26 Wang X, Wu Y, Li X, Liang S. Numerical investigation into evolution of crack and stress in residual coal pillars under the influence of longwall mining of the adjacent underlying coal seam. *Shock Vib*. 2019;2094378:1–18.
27 Shreedharan S, Kulatilake PHSW. Discontinuum-equivalent continuum analysis of the stability of tunnels in a deep coal mine using the distinct element method. *Rock Mech Rock Eng*. 2016;49(5):1903–1922.
28 Hoek E, Kaiser PK, Bawden WF. *Support of Underground Excavations in Hard Rock*. CRC Press; 2000.
29 Diederichs MS, Kaiser PK, Eberhardt E. Damage initiation and propagation in hard rock during tunnelling and the influence of near-face stress rotation. *Int J Rock Mech Min Sci*. 2004;41:785–812.
30 Diederichs MS. Manuel Rocha Medal recipient Rock fracture and collapse under low confinement conditions. *Rock Mech Rock Eng*. 2003;36:339–381.
31 Chen R. *In Situ and Laboratory Studies of Potash Deformation with Reference to Saskatchewan Potash*. Winnipeg, Manitoba: University of Manitoba; 1993. PhD Thesis.
32 Esterhuizen GS, Ellenberger JL. Effects of weak bands on pillar stability in stone mines: field observations and numerical model assessment. *Proceedings of the 26th International Conference on Ground Control in Mining, Morgantown, WV.*. 2007:336–342.
33 Kang HP, Lin J, Fan MJ. Investigation on support pattern of a coal mine roadway within soft rocks—a case study. *Int J Coal Geol*. 2015;140:31–40.
34 Bai JB, Wang XY, Yan S, Wu SX. Numerical study of failure mechanisms and control techniques for a gob-side yield pillar in the Sijiazhuang coal mine, China. *Rock Mech Rock Eng*. 2019;52(4):1231–1245.
35 Mortazavi A, Hassani FP, Shabani M. A numerical investigation of rock pillar failure mechanism in underground openings. *Comput Geotech*. 2009;36(5):619–697.
36 Kaiser PK, Kim B, Bewich RP, Valley B. Rock mass strength at depth and implication for pillar design. *Min Technol*. 2011;120(3):170–179.
37 Sinha S, Walton G. A progressive S-shaped yield criterion and its application to rock pillar behavior. *Int J Rock Mech Min Sci*. 2018;105:98–109.
38 Sinha S, Walton G. Application of micromechanical modeling to prediction of in-situ rock behavior. In: *Proceedings of 52nd US Rock Mechanics/Geomechanics Symposium, Seattle, WA*. 2018. Paper No. 265.
39 Itasca UDEC. *Version 6.0: Theory and Background*. Minneapolis, Minnesota: Itasca Consulting Group Inc.; 2014.
40 Sinha S, Walton G. A study on Bonded Block Model (BBM) complexity for simulation of laboratory-scale stress-strain behavior in granitic rocks. *Comput Geotech*. 2020;118:103363.
41 Jing L. A review of techniques, advances and outstanding issues in numerical modelling for rock mechanics and rock engineering. *Int J Rock Mech Min Sci*. 2003;40(3):283–353.
42 Bahrani N, Hadjigeorgiou J. Influence of stope excavation of drift convergence and support behavior: insights from 3D continuum and discontinuum models. *Rock Mech Rock Eng*. 2018;51(8):2395–2413.
43 Noorani R, Cai M. Simulation of dilation behavior of brittle rocks using a grain-based model. Montreal, Canada *Proceedings of the 13th ISRM International Congress of Rock Mechanics*. 2015:1–12.
44 Wang X, Cai M. A comprehensive parametric study of grain-based models for rock failure process simulation. *Int J Rock Mech Min Sci*. 2019;115:60–76.
45 Xue G, Gu C, Fang X, Wei T. A case study on large deformation failure mechanism and control techniques for soft rock roadways in tectonic stress areas. *Sustainability*. 2019;11(13):3510.
46 Yang SQ, Chen M, Jing HW, Chen KF, Meng B. A case study on large deformation failure mechanism of deep soft rock roadway in Xin'An coal mine. *China. Engineering Geology*. 2017;217:89–101.
47 Yang X, Wang E, Wang Y, Gao Y, Wang P. A study of the large deformation mechanism and control techniques for deep soft rock roadways. *Sustainability*. 2018;10(4):1100.
48 Sinha S, Walton G. Integration of a three-dimensional continuum model and a two-dimensional Bonded Block Model (BBM) for studying the damage process in a granite pillar at the Creighton Mine, Sudbury, Canada. *J Rock Mech Geotech Eng*. 2020. https://doi.org/10.1016/j.jrmge.2020.06.011.
49 Sinha S, Walton G. Modeling the behavior of a coal pillar rib using Bonded Block Models (BBMs) with emphasis on ground-support interaction. *Journal of Rock Mechanics and Geotechnical Engineering*. 2021. R1 submitted.
50 Walton G, Diederichs M, Punkkinen A, Whitmore J. Back analysis of a pillar monitoring experiment at 2.4 km depth in the Sudbury Basin, Canada. *Int J Rock Mech Min Sci*. 2016;85:33–51.
51 Alejano LR, Arzua J, Castro-Filgueira U, Malan F. Strapping of pillars with cables to enhance pillar stability. *J S Afr Inst Min Metall*. 2017;117:527–540.
52 Gao F, Stead D, Kang H. Simulation of roof shear failure in coal mine roadways using an innovative UDEC Trigon approach. *Comput Geotech*. 2014;61:33–41.
53 Gao F, Stead D, Elmo D. Numerical simulation of microstructure of brittle rock using a grain-breakable distinct element grain-based model. *Comput Geotech*. 2016;78:203–217.
54 Wang X, Cai M. Modeling of brittle rock failure considering inter-and intra-grain contact failures. *Comput Geotech*. 2018;101:224–244.
55 Liu H, Zhang K, Shao S, Ranjith PG. Numerical investigation on the mechanical properties of Australian Strathbogie granite under different temperatures using Discrete Element Method. *Rock Mech Rock Eng*. 2019;52(10):3719–3735.
56 Hudyma MR. *Rib Pillar Design in Open Stope Mining*. M.A.Sc. Thesis. The University of British Columbia; 1988.
57 Sjoberg J. Failure modes and pillar behavior in the Zinkgruvan mine. Santa Fe, New Mexico *Proceedings of the 33rd U.S. Rock Mechanics Symposium*. 1992:491–500.
58 Sinha S, Walton G. Numerical analyses of pillar behavior with variation in yield criterion, dilatancy, rock heterogeneity and length to width ratio. *Journal of Rock Mechanics and Geotechnical Engineering*. 2019;11(1):46–60.
59 Damjanac B, Board M, Lin M, Kicker D, Leem J. Mechanical degradation of emplacement drifts at Yucca Mountain—a modeling case study: Part II: lithophysal rock. *Int J Rock Mech Min Sci*. 2007;44(3):368–399.
60 Sinha S. *Advancing Continuum and Discontinuum Models of Brittle Rock Damage and Rock Support Interaction*. Golden, Colorado, US: Ph.D. Thesis, Colorado School of Mines; 2020.
61 Hajiabdolmajid V, Kaiser PK, Martin CD. Modelling brittle failure of rock. *Int J Rock Mech Min Sci*. 2002;39(6):731–741.
62 Hajiabdolmajid V, Kaiser PK, Martin CD. Mobilised strength components in brittle failure of rock. *Geotechnique*. 2003;53(3):327–336.
63 Martin CD, Chandler NA. The progressive fracture of Lac du Bonnet granite. *Int J Rock Mech Min Sci Geomech Abstr*. 1994;31(6):643–659.
64 Zhao X, Cai M, Cai M. Considerations of rock dilation on modeling failure and deformation of hard rocks—a case study of the mine-by test tunnel in Canada. *Journal of Rock Mechanics and Geotechnical Engineering*. 2010;2(4):338–349.
65 Lee KH, Lee IM, Shin YJ. Brittle rock property and damage index assessment for predicting brittle failure in excavations. *Rock Mech Rock Eng*. 2012;45(2):251–257.
66 Renani HR, Martin CD. Modeling the progressive failure of hard rock pillars. *Tunn Undergr Space Technol*. 2018;74:71–81.
67 Walton G, Diederichs MS, Alejano LR, Arzúa J. Verification of a laboratory-based dilation model for in situ conditions using continuum models. *Journal of Rock Mechanics and Geotechnical Engineering*. 2014;6(6):522–534.
68 Luke N. *Analysis and Interpretation of In-Situ Rock Bolt Pull Tests in Hard Rock Mines. Master Thesis*. Toronto, Canada: University of Toronto; 2016.
69 Mayer JM, Stead D. Exploration into the causes of uncertainty in UDEC grain boundary models. *Comput Geotech*. 2017;82:110–123.
70 Walton G. Initial guidelines for the selection of input parameters for cohesion-weakening-friction-strengthening (CWFS) analysis of excavations in brittle rock. *Tunn Undergr Space Technol*. 2019;84:189–200.
71 Renani HR, Martin CD. Cohesion degradation and friction mobilization in brittle failure of rocks. *Int J Rock Mech Min Sci*. 2018;106:1–3.
72 Alejano LR, González J, Muralha J. Comparison of different techniques of tilt testing and basic friction angle variability assessment. *Rock Mech Rock Eng*. 2012;45(6):1023–1035.
73 Christianson M, Board M, Rigby D. UDEC simulation of triaxial testing of lithophysal tuff. In: *Proceedings of 41st U.S. Rock Mechanics/Geomechanics Symposium, Golden, Colorado*. 2006. Paper No. 968.
74 Farahmand K, Vazaios I, Diederichs MS, Vlachopoulos N. Investigating the scale-dependency of the geometrical and mechanical properties of a moderately jointed rock using a synthetic rock mass (SRM) approach. *Comput Geotech*. 2018;95:162–179.
75 Stavrou A, Murphy W. Quantifying the effects of scale and heterogeneity on the confined strength of micro-defected rocks. *Int J Rock Mech Min Sci*. 2018;102:131–143.
76 Hoek E. *Support for very weak rock associated with faults and shear zones. Proceedings of Rock Support and Reinforcement Practice in Mining*. Rotterdam: Balkema; 1999:19–32.
77 Arzúa J, Alejano LR. Dilation in granite during servo-controlled triaxial strength tests. *Int J Rock Mech Min Sci*. 2013;61:43–56.
78 Walton G. Scale effects observed in compression testing of Stanstead granite including post-peak strength and dilatancy. *Geotech Geol Eng*. 2018;36(2):1091–1111.
79 Lajtai EZ. Microscopic fracture processes in a granite. *Rock Mech Rock Eng*. 1998;31(4):237–250.
80 Li D, Li CC, Li X. Influence of sample height-to-width ratios on failure mode for rectangular prism samples of hard rock loaded in uniaxial compression. *Rock Mech Rock Eng*. 2011;44(3):253–267.
81 Chen L, Wang CP, Liu JF, et al. Damage and plastic deformation modeling of Beishan granite under compressive stress conditions. *Rock Mech Rock Eng*. 2015;48(4):1623–1633.
82 Gray P. *Bearing plates: new developments in the unsung heroes of ground support. Proceedings of Coal Operators' Conference*. University of Wollongong & the Australian Institute of Mining and Metallurgy, Australia; 1998:167–178.
83 Oliveira D, Diederichs M. Tunnel support for stress induced failures in Hawkesbury Sandstone. *Tunn Undergr Space Technol*. 2017;64:10–23.
84 Walton G. *Improving Continuum Models for Excavations in Rock Masses under High Stress through an Enhanced Understanding of Post-yield Dilatancy*. Kingston, Canada: Ph.D. Thesis. Queen's University; 2014.

85 Kaiser PK. *Deformation-based support selection for tunnels in strainburst-prone ground. Proceedings of the Seventh International Conference on Deep and High Stress Mining.* Sudbury: Canada; 2014:227–240.
86 Martin CD, Kaiser PK, McCreath DR. Hoek-Brown parameters for predicting the depth of brittle failure around tunnels. *Can Geotech J*. 1999;36(1):136–151.
87 Ghazvinian E, Diederichs MS, Quey R. 3D random Voronoi grain-based models for simulation of brittle rock damage and fabric-guided micro-fracturing. *Journal of Rock Mechanics and Geotechnical Engineering*. 2014;6(6):506–521.